

Challenges and Progress in Lead-Free Halide Double Perovskite Solar Cells

Fuxiang Ji, Gerrit Boschloo, Feng Wang,* and Feng Gao

Lead-free halide double perovskites (HDPs) with a chemical formula of $A_2B^+B^{3+}X_6$ are booming as attractive alternatives to solve the toxicity issue of lead-based halide perovskites (APbX₃). HDPs show excellent stability, a wide range of possible combinations, and attractive optoelectronic features. Although a number of novel HDPs have been studied, the power conversion efficiency of the state-of-the-art double perovskite solar cell is still far inferior to that of the dominant Pb-based ones. Understanding the fundamental challenges is essential for further increasing device efficiency. In this review, HDPs with attractive electronic and optical properties are focused on, and current challenges in material properties and device fabrication that limit high-efficiency photovoltaics are analyzed. Finally, the promising approaches and views to overcome these bottlenecks are highlighted.

1. Introduction

Lead-based metal halide perovskites have brought a revolution in photovoltaics in the last few years with a dramatic increase in the power conversion efficiency (PCE) from 3.8% in 2009 to 25.7% in 2022.^[1,2] The incredible PCE improvement is mainly due to their remarkable optical and electrical properties, including suitable and tunable direct bandgap, high absorption coefficient, small exciton binding energy, long carrier diffusion length and lifetime, high carrier mobility, high defect tolerance, etc.^[3–7] Besides, low-cost and printable devices have further prospered this fantastic technology.^[8] Despite these exciting achievements, Pb-based perovskites suffer from two significant issues: toxicity and long-term instability.^[9,10] The toxicity issue comes from the Pb which can induce detrimental environmental and health

effects in the case of leakage. For long-term instability, Pd-based perovskites are susceptible to degradation after exposure to light, oxygen, moisture, or heat, ascribed to polymorphic transformation, hydration, or decomposition. Both of these issues hinder their further development and commercialization.


A straightforward way to address the instability and Pb toxicity issues is to develop stable and lead-free perovskites. The first substitution candidate is Sn²⁺, as it is in the same group of the periodic table as Pb with similar lone pairs. As expected, these Sn²⁺-based materials maintain the 3D perovskite structure and exhibit relatively high PCE.^[11] A critical issue for

Sn-based perovskites is the easy oxidization of Sn²⁺ to Sn⁴⁺. Moreover, Sn²⁺ might be also harmful to the human body due to the strong acidification induced by the SnI₂.^[9] Instead of Sn²⁺, more stable elements such as Ag⁺, Na⁺, Bi³⁺, Sb³⁺, In³⁺, Fe³⁺, Ti⁴⁺, Pd⁴⁺, etc. were employed to form various novel lead-free perovskites or perovskite derivatives, including A₃B³⁺X₉,^[12] A₂B⁴⁺X₆,^[13] B⁴⁺B³⁺X₇,^[14] A₂B²⁺B³⁺X₅,^[15] and halide double perovskites (HDPs) A₂B⁺B³⁺X₆^[16] (A = Cs⁺, MA⁺, FA⁺; B = metal ions; X = Cl⁻, Br⁻, I⁻). Unfortunately, except for HDPs (A₂B⁺B³⁺X₆), the crystal dimensionalities of other materials are 2D or 0D, different from the 3D structure of connected BX₆ octahedra in Pb-based perovskites. Generally, the drawbacks of the low structural dimensionality (0D–2D) are poor carrier transport, high carrier effective masses, and exciton binding energies, limiting their applications in photovoltaics. Therefore, lead-free perovskite candidates with high structure dimensionality are more favorable for high-efficiency photovoltaics.

Recently, HDPs (A₂B⁺B³⁺X₆) with 3D perovskite structure and exciting optoelectronic properties are becoming one of the most promising Pb-free perovskite candidates in photovoltaic applications. The benchmark HDP Cs₂AgBiBr₆ for solar cells was first reported in 2017.^[17] Afterward, this material has been explored for various photoelectric applications, including photodetectors,^[18] X-ray detectors,^[19] and photocatalysis.^[20] Encouraged by the great success of Cs₂AgBiBr₆ in photoelectric applications, a series of novel HDPs have been successfully synthesized. Unfortunately, they still show little success in solar cells, although some of them possess attractive optical and electrical features. Meanwhile, the record PCE for the benchmark HDP Cs₂AgBiBr₆ is only around 6.37%, still far behind the Pb-based perovskite solar cells.^[21] Although there are many reviews focusing on the benchmark HDP Cs₂AgBiBr₆ for different photoelectric applications, a systematic review that focuses on

F. Ji, F. Wang, F. Gao
Department of Physics, Chemistry, and Biology (IFM)
Linköping University
SE-58 183 Linköping, Sweden
E-mail: feng.wang@liu.se

F. Ji, G. Boschloo
Department of Chemistry-Ångström Laboratory
Physical Chemistry
Uppsala University
SE-751 20 Uppsala, Sweden

 The ORCID identification number(s) for the author(s) of this article can be found under <https://doi.org/10.1002/solr.202201112>.

© 2023 The Authors. Solar RRL published by Wiley-VCH GmbH. This is an open access article under the terms of the Creative Commons Attribution-NonCommercial-NoDerivs License, which permits use and distribution in any medium, provided the original work is properly cited, the use is non-commercial and no modifications or adaptations are made.

DOI: 10.1002/solr.202201112

the challenges limiting HDP-based photovoltaics is currently missing.^[22–25]

In this review, we first summarize the optical and electrical properties of various HDPs with the 3D structure to better understand and explore their full potential in photovoltaics. For clarity, these HDP candidates are categorized by their trivalent metal ions: Bi-based, Sb-based, In-based, Fe-based, Tl-based, and Au-based. Then, we highlight the main challenges limiting the photovoltaic application from both the materials development and device fabrication. The challenges of the materials include large bandgap, indirect bandgap nature, parity-forbidden transitions, low electronic dimensionality, weak or no photoluminescence (PL), short carrier diffusion length, etc. The challenges in device fabrication include the difficulties to fabricate and dope/alloy HDP films, contact issues, high defect density in thin films, etc. Finally, we emphasize the recent efforts and provide our views on addressing these challenges.

2. What are HDPs?

Perovskites are generally applied to the class of compounds with the same crystal structure as calcium titanate mineral CaTiO_3 . The general chemical formula for the Pb halide perovskites can be described as APbX_3 , where A is organic or inorganic cations (e.g., methylammonium (MA^+), formamidinium (FA^+), Cs^+), B is Pb^{2+} , and X is a halogen (I^- , Br^- , Cl^-). The crystal

structure of APbX_3 perovskites is shown in **Figure 1a**, in which Pb^{2+} bonds with six X halogens to form $[\text{PbX}_6]^{4-}$ octahedra connected by the corner-sharing mode in 3D, and A-site cations occupy the cavities created by eight $[\text{PbX}_6]^{4-}$ octahedra.

HDPs with the formula of $\text{A}_2\text{B}^+\text{B}^{3+}\text{X}_6$ can be formed by using one monovalent cation B^+ and one trivalent B^{3+} to replace two Pb^{2+} . The double perovskites have a similar 3D structure as Pb perovskites with alternating $[\text{B}^+\text{X}_6]^{5-}$ and $[\text{B}^{3+}\text{X}_6]^{3-}$ octahedra, and A-site cations are in the cavities formed by octahedra (**Figure 1b**). It is worth noting that HDPs are usually non/less toxic (except Tl-based compounds) and much more stable compared with Pb-based perovskites. Equally important, two different B-site cations enable access to a wide range of possible combinations and rich substitutional chemistry. As shown in **Figure 1c**, we summarize the elements that have been successfully employed to synthesize HDPs for potential photovoltaics. The selection of A cation and X anion is relatively narrow, in which A cation is mainly Cs^+ and CH_3NH_3^+ (MA^+), and X anion is mainly Cl^- , Br^- , and I^- . In contrast, the choice of B-site cations is more flexible, including Ag^+ , Na^+ , Li^+ , Au^+ , Bi^{3+} , Sb^{3+} , In^{3+} , Fe^{3+} , Tl^{3+} , etc. Additional B^{3+} cations such as rare-earth ions are not marked here because the corresponding HDPs are more attractive for phosphors or light-emitting diodes.^[26] By simply permuting and combining these elements, hundreds of HDPs can be obtained. Meanwhile, two different B-site metal ions provide many chances for alloying and doping in HDPs (**Figure 1c**) by many elements, further expanding the large family

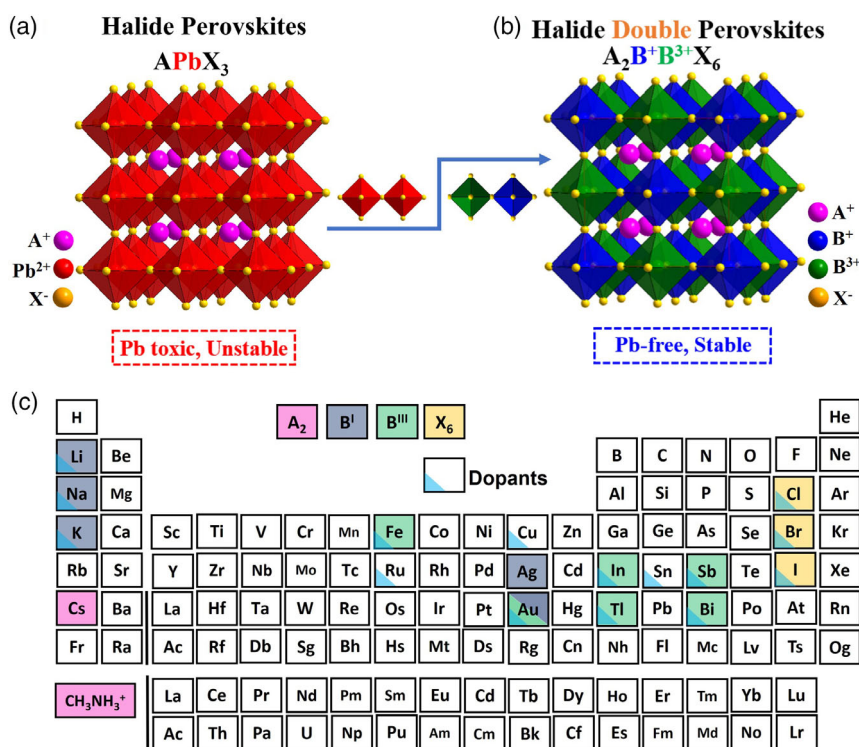


Figure 1. a,b) Schematic view of B^+/B^{3+} cation substitution from Pb halide perovskites (APbX_3) to double perovskites ($\text{A}_2\text{B}^+\text{B}^{3+}\text{X}_6$). c) Elements form HDPs with composition $\text{A}_2\text{B}^+\text{B}^{3+}\text{X}_6$. An element is colored if at least one compound with a double perovskite structure containing that element has been synthesized. The different colors specify the site occupied by the element, according to the legend at the top. The triangular blue color tags indicate the applied dopants in HDPs. This table only considers HDPs with potential for photovoltaic applications. The element Au can form double perovskite $\text{A}_2\text{Au}_2\text{X}_6$ with alternating compressed and elongated AuX_6 octahedra.

of HDPs and offering immense opportunities for HDP-based photovoltaics.

It should be noted that not all of these possible HDPs are stable compounds. Generally, the crystallographic stability of the perovskite structure can be predicted by the Goldschmidt tolerance factor t (Equation (1))^[27] and the octahedral factor μ (Equation (2))^[28] Recently, Bartel and co-workers presented a new tolerance factor τ with high prediction accuracy (Equation (3)).^[29] The parameters t , μ , and τ are calculated through the following equations

$$t = \frac{(R_A + R_x)}{\sqrt{2}(R_B + R_X)} \quad (1)$$

$$\mu = \frac{R_B}{R_X} \quad (2)$$

$$\tau = \frac{R_x}{R_B} - n_A \left(n_A - \frac{R_A/R_B}{\ln(R_A/R_B)} \right) \quad (3)$$

where n_A is the oxidation state of A, $R_A > R_B$ by definition, and R_A , R_B , and R_X represent the ionic radii of A, B, and X ions, respectively. Considering that HDPS contain two different B cations, R_B refers to the average radius of B^+ and B^{3+} cations. In principle, to form a stable perovskite structure, the Goldschmidt tolerance factor t , tolerance factor τ , and octahedral factor μ should be in the range of $0.81 < t < 1.11$, $\tau < 4.18$, and $0.41 < \mu < 0.90$, respectively.^[28] We summarize these three critical factors, t , τ , and μ , for HDP candidates for photovoltaics in **Figure 2** and **Table 1**. In Figure 2a, all these HDPs have a suitable Goldschmidt tolerance factor t value between 0.81 and 1.11, implying that only limited structural prediction information

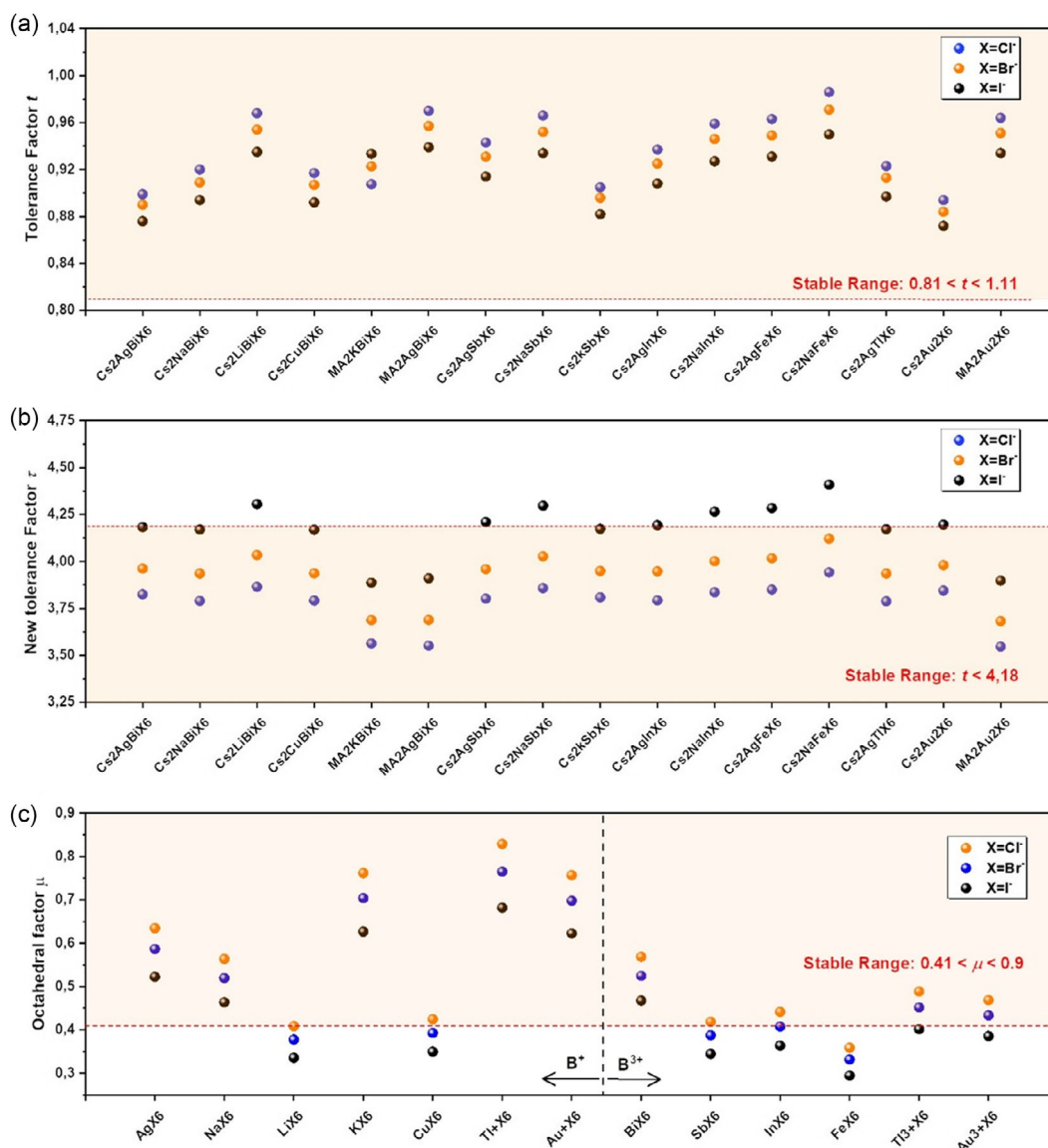


Figure 2. a) Goldschmidt tolerance factor t , b) new tolerance factor τ , and c) octahedral factor μ for HDPs. The orange region demonstrates the theoretically stable range.

Table 1. Goldschmidt tolerance factor t , new tolerance factor τ , and octahedral factor μ of HDPs.

| Composition | Goldschmidt tolerance factor t | New tolerance factor τ | Octahedra | Octahedral factor μ |
|-------------------------------------|----------------------------------|-----------------------------|------------------------------------|-------------------------|
| Cs ₂ AgBiI ₆ | 0.877 | 4.183 | [AgI ₆] ⁵⁻ | 0.523 |
| Cs ₂ AgBiBr ₆ | 0.890 | 3.962 | [AgBr ₆] ⁵⁻ | 0.587 |
| Cs ₂ AgBiCl ₆ | 0.999 | 3.825 | [AgCl ₆] ⁵⁻ | 0.635 |
| MA ₂ AgBiI ₆ | 0.939 | 3.910 | [NaI ₆] ⁵⁻ | 0.464 |
| MA ₂ AgBiBr ₆ | 0.957 | 3.689 | [NaBr ₆] ⁵⁻ | 0.520 |
| MA ₂ AgBiCl ₆ | 0.970 | 3.552 | [NaCl ₆] ⁵⁻ | 0.564 |
| Cs ₂ NaBiI ₆ | 0.895 | 4.170 | [LiI ₆] ⁵⁻ | 0.336 |
| Cs ₂ NaBiBr ₆ | 0.910 | 3.936 | [LiBr ₆] ⁵⁻ | 0.378 |
| Cs ₂ NaBiCl ₆ | 0.920 | 3.790 | [LiCl ₆] ⁵⁻ | 0.409 |
| Cs ₂ LiBiI ₆ | 0.935 | 4.305 | [Kl ₆] ⁵⁻ | 0.627 |
| Cs ₂ LiBiBr ₆ | 0.954 | 4.034 | [KBr ₆] ⁵⁻ | 0.704 |
| Cs ₂ LiBiCl ₆ | 0.968 | 3.865 | [KCl ₆] ⁵⁻ | 0.762 |
| Cs ₂ CuBiI ₆ | 0.892 | 4.169 | [CuI ₆] ⁵⁻ | 0.350 |
| Cs ₂ CuBiBr ₆ | 0.907 | 3.937 | [CuBr ₆] ⁵⁻ | 0.393 |
| Cs ₂ CuBiCl ₆ | 0.917 | 3.792 | [CuCl ₆] ⁵⁻ | 0.425 |
| MA ₂ KBiI ₆ | 0.908 | 3.887 | [TlI ₆] ⁵⁻ | 0.682 |
| MA ₂ KBiBr ₆ | 0.923 | 3.688 | [TlBr ₆] ⁵⁻ | 0.765 |
| MA ₂ KBiCl ₆ | 0.933 | 3.563 | [TlCl ₆] ⁵⁻ | 0.829 |
| Cs ₂ AgSbI ₆ | 0.914 | 4.210 | [AuI ₆] ⁵⁻ | 0.623 |
| Cs ₂ AgSbBr ₆ | 0.931 | 3.959 | [AuBr ₆] ⁵⁻ | 0.698 |
| Cs ₂ AgSbCl ₆ | 0.944 | 3.802 | [AuCl ₆] ⁵⁻ | 0.757 |
| Cs ₂ NaSbI ₆ | 0.934 | 4.297 | [BiI ₆] ³⁻ | 0.468 |
| Cs ₂ NaSbBr ₆ | 0.953 | 4.027 | [BiBr ₆] ³⁻ | 0.525 |
| Cs ₂ NaSbCl ₆ | 0.966 | 3.858 | [BiCl ₆] ³⁻ | 0.569 |
| Cs ₂ kSbI ₆ | 0.882 | 4.173 | [SbI ₆] ³⁻ | 0.345 |
| Cs ₂ kSbBr ₆ | 0.896 | 3.949 | [SbBr ₆] ³⁻ | 0.388 |
| Cs ₂ kSbCl ₆ | 0.905 | 3.809 | [SbCl ₆] ³⁻ | 0.419 |
| Cs ₂ AgInI ₆ | 0.909 | 4.193 | [InI ₆] ³⁻ | 0.364 |
| Cs ₂ AgInBr ₆ | 0.925 | 3.947 | [InBr ₆] ³⁻ | 0.408 |
| Cs ₂ AgInCl ₆ | 0.937 | 3.793 | [InCl ₆] ³⁻ | 0.442 |
| Cs ₂ NaInI ₆ | 0.928 | 4.265 | [FeI ₆] ³⁻ | 0.295 |
| Cs ₂ NaInBr ₆ | 0.946 | 4.001 | [FeBr ₆] ³⁻ | 0.332 |
| Cs ₂ NaInCl ₆ | 0.959 | 3.836 | [FeCl ₆] ³⁻ | 0.359 |
| Cs ₂ AgFeI ₆ | 0.931 | 4.284 | [TlI ₆] ³⁻ | 0.402 |
| Cs ₂ AgFeBr ₆ | 0.949 | 4.017 | [TlBr ₆] ³⁻ | 0.452 |
| Cs ₂ AgFeCl ₆ | 0.963 | 3.850 | [TlCl ₆] ³⁻ | 0.489 |
| Cs ₂ NaFeI ₆ | 0.951 | 4.409 | [AuI ₆] ³⁻ | 0.386 |
| Cs ₂ NaFeBr ₆ | 0.971 | 4.121 | [AuBr ₆] ³⁻ | 0.434 |
| Cs ₂ NaFeCl ₆ | 0.986 | 3.942 | [AuCl ₆] ³⁻ | 0.469 |
| Cs ₂ AgTlI ₆ | 0.897 | 4.172 | | |
| Cs ₂ AgTlBr ₆ | 0.913 | 3.936 | | |
| Cs ₂ AgTlCl ₆ | 0.924 | 3.788 | | |
| Cs ₂ AuAuI ₆ | 0.872 | 4.196 | | |
| Cs ₂ AuAuBr ₆ | 0.884 | 3.980 | | |
| Cs ₂ AuAuCl ₆ | 0.894 | 3.845 | | |

Table 1. Continued.

| Composition | Goldschmidt tolerance factor t | New tolerance factor τ | Octahedra | Octahedral factor μ |
|-------------------------------------|----------------------------------|-----------------------------|-----------|-------------------------|
| MA ₂ AuAuI ₆ | 0.934 | 3.898 | | |
| MA ₂ AuAuBr ₆ | 0.951 | 3.682 | | |
| MA ₂ AuAuCl ₆ | 0.964 | 3.547 | | |

can be obtained from this parameter. Interestingly, the new tolerance factors for most I-based double perovskites are above 4.81, which can explain the feature of theoretically unstable. Furthermore, the octahedral factor μ of some BX₆ octahedra, particularly for I-based or Br-based ones, exhibits a small value below 0.41 (Figure 2c), further confirming their poor structure stability.

However, these three factors cannot fully predict the crystallographic stability of HDPs. For example, although the octahedral factor μ of [FeCl₆]³⁻ is only 0.36, both Cs₂AgFeCl₆ and Cs₂NaFeCl₆ are stable materials.^[30] Conversely, Cs₂CuBiCl₆ and Cs₂NaBiI₆ have appropriate Goldschmidt tolerance factor t , octahedral factor μ , and octahedral factor μ , but they have not been synthesized successfully. The reason can be understood by the decomposition energy demonstrated recently by the first-principles density functional theory (DFT) calculations. Mitzi and co-workers found that Cu⁺-based HDPs show negative decomposition energy, indicating that they would spontaneously decompose to CsCu₂X₃.^[31] Similarly, Cs₂NaBiI₆ tends to form the thermodynamically more stable by-product Cs₃Bi₂I₉. Therefore, it is necessary to combine Goldschmidt tolerance factor t , octahedral factor μ , octahedral factor μ , and decomposition energy to better predict the structural stability of new HDPs.

3. Optoelectronic Properties of HDPs

Up to now, more than 350 different HDPs have been successfully synthesized, and at least around 600 compounds have not been investigated.^[26] It is highly expected a great potential of HDPs for kinds of optoelectronic applications. Since the first report of Cs₂AgBiBr₆ for solar cells in 2017, an increasing number of novel HDPs with exciting optoelectronic properties have emerged. In this section, we review their fundamental optical and electrical properties by categorizing them as Bi-based, Sb-based, In-based, Fe-based, Tl-based, and Au-based HDPs.

3.1. Bi-Based HDPs

Bi³⁺ has a similar 6s²6p⁰ electronic configuration as Pb²⁺, which is important for high light absorption and long carrier lifetimes.^[32] Up to now, Bi-based HDPs is one of the most promising group for photovoltaics, including Cs₂AgBiBr₆, Cs₂AgBiCl₆, Cs₂AgBiI₆ (nanocrystals), MA₂AgBiBr₆, Cs₂NaBiCl₆, MA₂KBiCl₆, Cs₂LiBiCl₆, etc.^[16,33–37] Amongst, the benchmark HDP for photovoltaics is Cs₂AgBiBr₆, which crystallizes in the cubic system with a space group of Fm $\bar{3}$ m at room temperature. Its conduction band minimum (CBM) is mainly

derived from Bi 6*p*–Br 4*p* antibonding states at the *L* point, and the valence band maximum (VBM) comes from Ag 4*d*–Br 4*p* antibonding states at the *X* point, as shown in **Figure 3a,b**.^[38] The optical bandgap of Cs₂AgBiBr₆ crystal calculated by UV–vis absorption spectrum shows various values in the range of 1.95–2.19 eV (Figure 3c).^[16,33,39] It is worth noting that unusual black Cs₂AgBiBr₆ crystals with a smaller optical bandgap of 1.69–1.72 eV were also reported, which could be related to the increased Ag–Bi disorder in the structure.^[39,40] A key issue for the application of Cs₂AgBiBr₆ in solar cells was its poor solubility in common organic solvents which is critical for low-cost device fabrication. This issue was solved by Bein and co-workers by dissolving precursor materials in hot dimethyl sulfoxide (DMSO) (75 °C). Figure 3d shows a typical UV–vis absorption spectrum of Cs₂AgBiBr₆ thin films, which can be separated into three regions.^[41] One is a flat and high absorption range at lower wavelengths below 350 nm, attributed to the direct bandgap absorption. A characteristic and strong peak at around 438 nm contributes more than 20% of the overall light absorption of Cs₂AgBiBr₆ films. This absorption should come from the optical transition from ¹S₀ ground state to the triplet ³P₁ excited state of Bi³⁺ in Cs₂AgBiBr₆.^[42] The third region is a weak and broad absorption region at a higher wavelength with an edge at around 610 nm, which arises from the indirect bandgap absorption. The exciton binding energy of Cs₂AgBiBr₆ was calculated to be 268 meV from the absorption edge at the direct transition using the Elliott model.^[43]

The PL of Cs₂AgBiBr₆ exhibits a broad peak centered at 1.87 eV at room temperature and a relatively narrow peak at 1.98 eV at 22.6 K (Figure 3e).^[16] The origin of the PL emission of Cs₂AgBiBr₆ is still under debate, possibly assigned to either the spatially localized color centers or the band-to-band emission.^[39,44,45] Due to the indirect bandgap nature, the measured PL quantum yield (PLQY) is only around 0.08%.^[46] Besides PL, the carrier lifetime and diffusion length are also crucial for evaluating the potential photovoltaic application. Figure 3f shows the time-resolved room-temperature PL (TRPL) of Cs₂AgBiBr₆ powders and single crystals; both exhibit a fast initial drop followed by a slower decay.^[16] The very fast decay process (50–150 ns) may originate from the trap, surface-state emission, or the lifetime of charge carriers. The long PL decay time of around 600 ns might result from the fundamental recombination of Cs₂AgBiBr₆ or the detrapping of charges in shallow states.^[16,47] By TRPL experiments, an average photoexcitation mobility was estimated to be $0.37 \pm 0.15 \text{ cm}^2 \text{ V}^{-1} \text{ s}^{-1}$, and the photoexcitation diffusion length for both electrons and holes was around $\approx 110 \pm 20 \text{ nm}$ in Cs₂AgBiBr₆ thin films based on the PL quenching model.^[48] Impressively, a super long carrier lifetime of 1.4 μs in Cs₂AgBiBr₆ thin film was measured through transient absorption spectroscopy,^[49] suggesting that the transport properties in Cs₂AgBiBr₆ could support thicker active layers. In Cs₂AgBiBr₆ crystals, the carrier diffusion length can even reach 1 μm measured by stroboscopic scattering microscopy.^[50] This value is much higher than that in the thin film, which could be

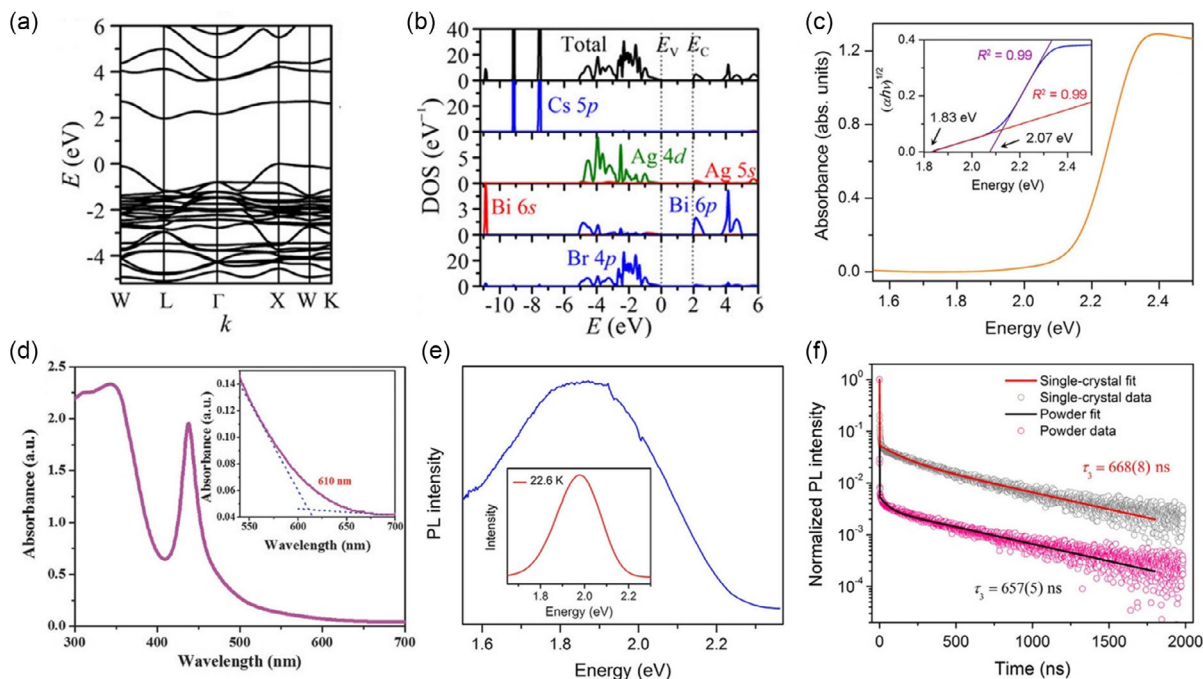


Figure 3. a) Band structures and b) total and projected density of states (DOSs) of Cs₂AgBiBr₆ calculated with the HSE + SOC methods. Reproduced with permission.^[38] Copyright 2016, Wiley-VCH. c) Absorbance spectrum of Cs₂AgBiBr₆ powder. Inset: Tauc plot showing the characteristics of an indirect bandgap. d) Typical absorption spectrum of Cs₂AgBiBr₆ films with the inset showing the absorption onset at 610 nm. (d) Reproduced with permission under the terms of the Creative Commons CC BY license.^[41] Copyright 2017, The Authors. Published by Wiley-VCH. e) Steady-state room-temperature PL spectrum of a powdered Cs₂AgBiBr₆ sample upon 500 nm excitation. Inset: low-temperature PL spectrum. f) Time-resolved room-temperature PL and fits for the PL decay time (τ) in powder and single-crystal samples. (c,e,f) Reproduced with permission.^[16] Copyright 2016, American Chemical Society.

understood by the reduced defect density in single crystal. Moreover, $\text{Cs}_2\text{AgBiBr}_6$ also processes relatively low carrier effective masses favorable for efficient charge transport and extraction.^[22] Another attractive property of $\text{Cs}_2\text{AgBiBr}_6$ is its excellent moisture, light, and thermal stability. It does not show any decomposition after storing in an ambient environment for 240 days or irradiating with a white LED lamp (0.75 Sun) under N_2 for 30 days or heating below 430°C .^[16] A hybrid HDP $\text{MA}_2\text{AgBiBr}_6$ with an indirect bandgap of 2.02 eV has been synthesized by using organic cation MA^+ to replace Cs^+ .^[34] Notably, the formation of $\text{MA}_2\text{AgBiBr}_6$ relies on additional MAPbBr_3 crystals as a seed, and its absence will yield layered $\text{MA}_3\text{Bi}_2\text{Br}_9$ crystals instead.

I-based double perovskites are particularly interesting for single-junction solar cells, as they potentially show smaller bandgaps than that of Br- and Cl-based ones. However, the successful synthesis of I-based double perovskites is rare. Take $\text{Cs}_2\text{AgBiI}_6$ as an example; its crystals or thin films have not been successfully synthesized so far, even though it has a suitable tolerance and octahedral factors. This is mainly because its byproduct $\text{Cs}_3\text{Bi}_2\text{I}_9$ is more thermodynamically stable.^[38] Interestingly, $\text{Cs}_2\text{AgBiI}_6$ nanocrystals were obtained through the anion exchange method. Nevertheless, these $\text{Cs}_2\text{AgBiI}_6$ nanocrystals are easily decomposed into $\text{Cs}_3\text{Bi}_2\text{I}_9$ nanocrystals after being exposed to air for several days.^[51] By replacing I^- with Cl^- , a

much more stable compound $\text{Cs}_2\text{AgBiCl}_6$ with an indirect bandgap of 2.77 eV was obtained.^[33] Besides $\text{Cs}_2\text{AgBiX}_6$ ($\text{X} = \text{Cl}, \text{Br}, \text{or I}$) compounds, other Bi-based HDPs such as $\text{Cs}_2\text{NaBiCl}_6$,^[52] $\text{MA}_2\text{KBiCl}_6$,^[36] and $\text{Cs}_2\text{LiBiCl}_6$,^[37] have also been reported with a large indirect bandgap of 3.25, 3.04, and 3.15 eV, respectively. Additional modifications are required to make these HDPs with large bandgaps suitable for potential photovoltaic applications.

3.2. Sb-Based HDPs

As Bi^{3+} and Sb^{3+} are isoelectronic ions, Sb^{3+} -based HDPs including $\text{Cs}_2\text{AgSbBr}_6$, $\text{Cs}_2\text{AgSbCl}_6$ and $\text{Cs}_2\text{NaSbCl}_6$ are also attractive for photovoltaics. Cheetham and co-workers have synthesized $\text{Cs}_2\text{AgSbBr}_6$ crystals through the hydrothermal method for the first time. Unfortunately, these crystals are accompanied by large amounts of secondary phases such as $\text{Cs}_3\text{Sb}_2\text{Br}_9$ and Cs_2AgBr_3 and unreacted AgBr .^[53] $\text{Cs}_2\text{AgSbBr}_6$ crystallizes in the same cubic space group $\text{Fm}\bar{3}\text{m}$ as $\text{Cs}_2\text{AgBiBr}_6$. Figure 4a,b show the band structure of $\text{Cs}_2\text{AgSbBr}_6$, where the CBM is dominated by antibonding Sb 5p–Br 4p interactions at the L point, and VBM primarily arises from Ag 4d and Br 4p orbital interactions at the X point.^[53] Different from $\text{Cs}_2\text{AgBiBr}_6$, the Sb^{3+} 5p–Br 4p antibonding states for the CBM are much lower than Bi^{3+} 6p–Br 4p

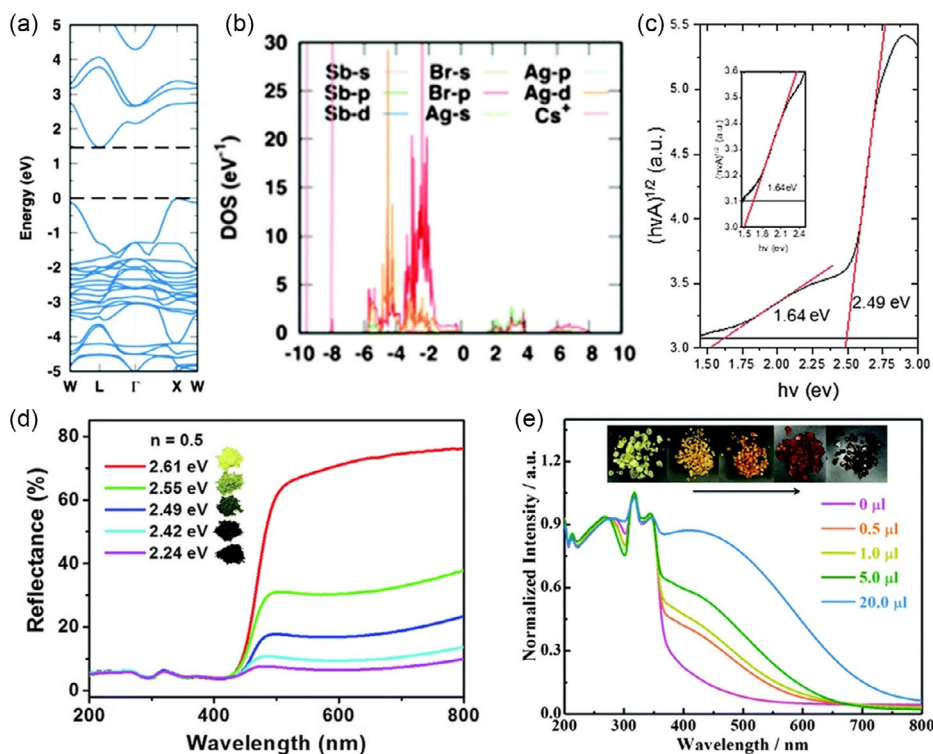


Figure 4. a) Calculated electronic band structures and b) projected density of states (PDOS) of $\text{Cs}_2\text{AgSbBr}_6$. c) Tauc plot derived from reflectance spectrum of a black sample of $\text{Cs}_2\text{AgSbBr}_6$ powder by assuming an indirect bandgap. Inset shows the indirect bandgap absorption edge. Reproduced with permission.^[53] Copyright 2019, Royal Society of Chemistry. d) UV-vis diffuse reflectance spectra of different as-prepared $\text{Cs}_2\text{AgSbCl}_6$ obtained by using different amounts of HCl (0.5, 0.75, 1.0, 1.25, and 1.5 mL) with variable visible light absorbance. Reproduced with permission.^[56] Copyright 2019, Royal Society of Chemistry. e) Steady-state absorption spectra (inset: images of the corresponding crystals under ambient light) of $\text{Cs}_2\text{NaBi}_{0.95}\text{Sb}_{0.05}\text{Cl}_6$ with different V_{HNO_3} in the hydrothermal reaction. Reproduced with permission.^[57] Copyright 2020, Royal Society of Chemistry.

states, resulting in a smaller bandgap with a shallow absorption edge at 1.64 eV followed by a sharp increase at 2.49 eV (Figure 4c). In addition, the effective mass of $\text{Cs}_2\text{AgSbBr}_6$ is smaller than that of $\text{Cs}_2\text{AgBiBr}_6$ indicated by DFT calculations,^[53] which is beneficial for larger charge carrier mobility. Meanwhile, $\text{Cs}_2\text{AgSbBr}_6$ thin films were also achieved by solution processing with annealing at 150 °C for 30 min. Similar to the synthesized crystals, the film also contains impurity phases of $\text{Cs}_3\text{Sb}_2\text{Br}_9$, Cs_2AgBr_3 , CsAgBr_2 , and AgBr . Interestingly, the phase-pure $\text{Cs}_2\text{AgSbBr}_6$ films have been successfully fabricated by annealing at a low temperature (135 °C) and a short time (5 mins).^[54] The optical bandgap of $\text{Cs}_2\text{AgSbBr}_6$ film is estimated to be 2.18 eV from UV–vis absorption. The fundamental optoelectronic properties of $\text{Cs}_2\text{AgSbBr}_6$ thin films, such as carrier lifetime and diffusion length, are still unclear.

By replacing Br^- with Cl^- , a more stable $\text{Cs}_2\text{AgSbCl}_6$ is formed, which crystallizes in the same $Fm\bar{3}m$ space group as $\text{Cs}_2\text{AgSbBr}_6$. The $\text{Cs}_2\text{AgSbCl}_6$ crystals show a shallow absorption edge at around 2.54 eV followed by a sharp increase in the absorption at 2.79 eV.^[55] Surprisingly, the crystal color of $\text{Cs}_2\text{AgSbCl}_6$ is black even though it has a very large bandgap. More interestingly, the color of $\text{Cs}_2\text{AgSbCl}_6$ powder can be continuously changed from yellow to near black by simply changing the concentration of precursor solution during hydrothermal routes.^[56] Sb-based/alloyed double perovskites show a similar color change along with different synthesis conditions. Recently, Gao and co-workers found that the reason should be related to the oxidation of Sb^{3+} to Sb^{5+} with the formation of oxygen anion or metal vacancies in the lattice to maintain the charge balance, which could break the local structure of the

double perovskite and change the bandgap. As a piece of evidence, they observed similar color changes in Sb-alloyed $\text{Cs}_2\text{NaBiCl}_6$ crystals by adding oxidant like diluted HNO_3 or H_2O_2 into the reaction solution (Figure 4e).^[57] Another possible reason for the absorption is the charge-transfer from Sb^{3+} to Sb^{5+} .

3.3. In-Based HDPs

In-based HDPs, mainly $\text{Cs}_2\text{AgInCl}_6$ and $\text{Cs}_2\text{NaInCl}_6$ compounds, have received much attention because of their direct bandgap character. Similar to other HDPs, no related I^- -based stable compounds were obtained so far, due to their small octahedral factor μ ($\mu < 0.41$) and/or thermodynamic instability. The pioneering work on $\text{Cs}_2\text{AgInCl}_6$ was reported by George Volonakis and co-workers in 2017.^[58] $\text{Cs}_2\text{AgInCl}_6$ crystallizes in a cubic unit cell with space group $Fm\bar{3}m$, and its CBM and VBM are both located at the Γ point, indicating the direct bandgap nature. The CBM mainly derives from the delocalized In 5s states, and the VBM mainly derives from Ag 4d and Cl 3p states (Figure 5a).^[59] The same even parity of the VBM and CBM makes the parity forbidden transitions occur at the Γ point.^[59] The optical transitions gradually become allowed as the k point changes from Γ to L point along with the introduction of the odd character, evident in the calculated dipole transition matrix element (Figure 5b).

The optical properties of $\text{Cs}_2\text{AgInCl}_6$ have been well investigated based on UV–vis and PL spectra. Figure 5c shows the UV–Vis absorption spectra of $\text{Cs}_2\text{AgInCl}_6$ single crystals, with a sharp absorption near 384 nm (3.2 eV) and a weak absorption

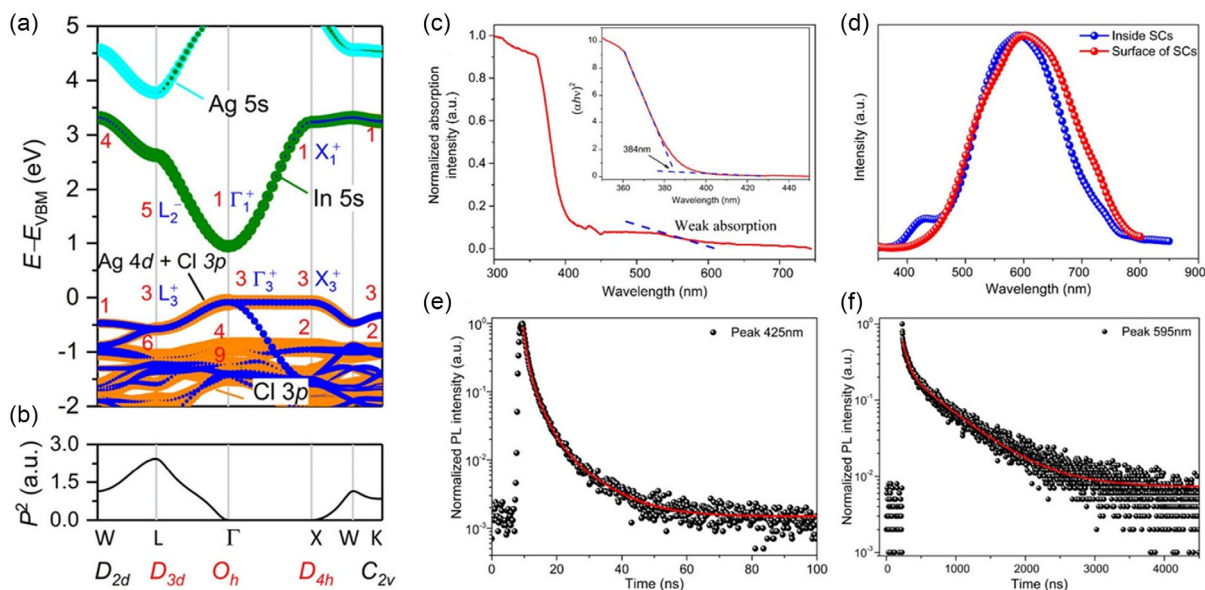


Figure 5. PBE calculated a) band structure and b) transition matrix elements for $\text{Cs}_2\text{AgInCl}_6$. The orange color corresponds to Cl 3p states, the green color to In 5s states, and the blue/cyan color to Ag 4d/5s states. Reproduced with permission.^[59] Copyright 2018, American Chemical Society. c) Absorption spectrum of $\text{Cs}_2\text{AgInCl}_6$ single crystals. Weak absorption was observed around 595 nm. Inset: Tauc plot showing the characteristics of a direct bandgap of 3.2 eV (384 nm). d) PL spectra (excited by 325 nm wavelength laser) of $\text{Cs}_2\text{AgInCl}_6$ crystal in the range of 350 to 800 nm. e, f) Time-resolved room-temperature PL decay of $\text{Cs}_2\text{AgInCl}_6$ single crystals monitored at 425 and 595 nm. Reproduced with permission.^[60] Copyright 2018, American Chemical Society.

near 595 nm (2.1 eV).^[60] The fundamental bandgap of $\text{Cs}_2\text{AgInCl}_6$ is 3.2 eV. For the PL spectra, only one broad PL peak centered at around 595 nm was observed on the crystal surface. In contrast, the bulk crystals show a strong, broad peak at 595 nm and a relatively weak satellite peak at 425 nm (Figure 5d).^[60] This satellite peak is explained by the free-exciton emission. The PL decay curve at 425 nm is composed of an initial fast component with a lifetime of 0.9 ns (64.3%), an intermediate component of 2.8 ns (31.8%), and a slow component of 9.8 ns (3.9%) (Figure 5e). The PL lifetime of $\text{Cs}_2\text{AgInCl}_6$ single crystals at 595 nm was much longer, with a fast component of 65.3 ns (97.0%) and a slow component of 566.9 ns (3.0%) (Figure 5f). Attractively, $\text{Cs}_2\text{AgInCl}_6$ shows excellent chemical, light, and thermal stability, without decomposition after storing it either in the dark at 55% relative humidity for 300 days or irradiated at 50 °C with an LED lamp at an intensity of 5.02 mW cm² for 48 h. The decomposition temperature of $\text{Cs}_2\text{AgInCl}_6$ is higher than 500 °C.^[60] Another stable In-based HDP, $\text{Cs}_2\text{NaInCl}_6$, also has a large direct bandgap of 3.7 eV.^[61] It is worth noting that these In-based HDPs exhibit rich and strong PL from self-trapped excitons (STEs),^[62] more attractive for phosphor and light-emitting diode (LED) applications.

3.4. Fe-Based HDPs

Recently, Fe-based HDPs $\text{Cs}_2\text{AgFeCl}_6$ and $\text{Cs}_2\text{NaFeCl}_6$ with excellent optical absorption properties attracted increasing attention. $\text{Cs}_2\text{AgFeCl}_6$ crystallizes in the space group of cubic $Fm\bar{3}m$ and was first reported by two independent groups at the same time.^[63,64]

The UV–vis absorbance spectrum indicates that $\text{Cs}_2\text{AgFeCl}_6$ crystals have an absorption edge at around 800 nm with an optical bandgap of around 1.62 eV, consistent with the black color of crystals (Figure 6a).^[64] To our knowledge, this is one of the lowest bandgaps for the reported Cl[−]-based HDPs. Unfortunately, there is no detectable PL in $\text{Cs}_2\text{AgFeCl}_6$ crystals even at low temperatures. The trap state densities for electrons and holes calculated by the space charge limited current (SCLC) model are 2.92×10^{10} and 1.02×10^{10} cm^{−3}, respectively (Figure 6b,c).^[30] The electron and hole mobility of $\text{Cs}_2\text{AgFeCl}_6$ single crystals is 15.3 and 64.6 cm² V^{−1} s^{−1}, respectively. The carrier diffusion length is found to be around 311 nm for $\text{Cs}_2\text{AgFeCl}_6$.^[30] In addition, $\text{Cs}_2\text{AgFeCl}_6$ displays superior stability with no detected signs of decomposition after 63 days storage in moisture air (RH = 50%) or 72 h soaking under air/light conditions (RH = 30%, white LED light with the intensity of 100 mW cm^{−2}).^[63]

Afterward, $\text{Cs}_2\text{NaFeCl}_6$ single crystals were synthesized with a bandgap of around 2.06 eV, larger than that of $\text{Cs}_2\text{AgFeCl}_6$.^[30] The absorption shows a sharp edge at about 600 nm and a weak broadband absorption at 750 nm (Figure 6d). Amongst, the redshift broadband absorption was explained by the formation of trapped excitons, which process less energy than free carriers.^[30] Similar to $\text{Cs}_2\text{AgFeCl}_6$, $\text{Cs}_2\text{NaFeCl}_6$ did not show any PL. The calculated trap state densities for electrons and holes in $\text{Cs}_2\text{NaFeCl}_6$ crystals are 8.35×10^{10} and 1.77×10^{10} cm^{−3}, respectively (Figure 6e,f).^[30] The electron and hole mobilities are 1.06 and 2.11 cm² V^{−1} s^{−1}, respectively. The carrier diffusion length of $\text{Cs}_2\text{NaFeCl}_6$ is only around 3.7 nm, much shorter than that of $\text{Cs}_2\text{AgFeCl}_6$.

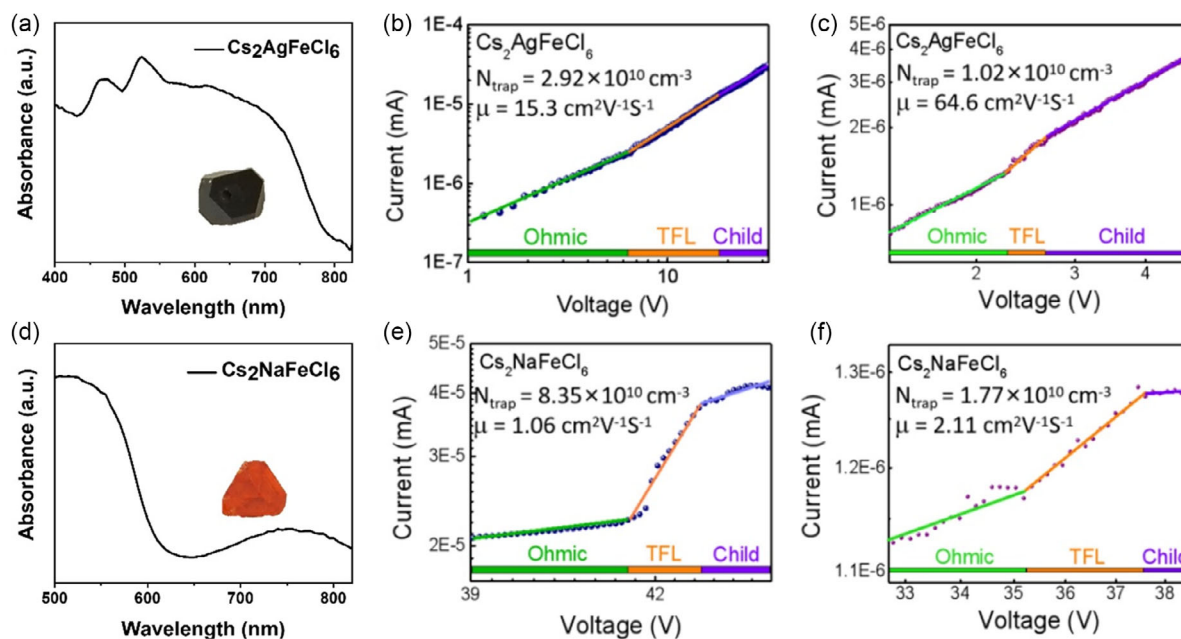


Figure 6. a) UV–vis spectra of $\text{Cs}_2\text{AgFeCl}_6$ single crystals (inset: images of $\text{Cs}_2\text{AgFeCl}_6$ single crystal under ambient light). Reproduced with permission under the terms of the Creative Commons CC BY license.^[64] Copyright 2021, the Author. Published by the Royal Society of Chemistry. b) Electron-associated current voltage curve measurement and c) hole-associated current voltage curve measurement of the $\text{Cs}_2\text{AgFeCl}_6$ single crystals for space charge limited current analysis. d) UV–vis spectra of $\text{Cs}_2\text{NaFeCl}_6$ single crystals (inset: images of $\text{Cs}_2\text{NaFeCl}_6$ single crystal under ambient light). e) Electron-associated current voltage curve measurement and f) hole-associated current voltage curve measurement of the $\text{Cs}_2\text{NaFeCl}_6$ single crystals for space charge limited current analysis. (b,c,e,f) Reproduced with permission.^[30] Copyright 2020, American Chemical Society.

3.5. Tl-Based HDPs

Tl, a more toxic element than Pb, can be employed as a B-site cation in HDPs. Without considering the toxicity, Tl-based HDPs $\text{Cs}_2\text{AgTlBr}_6$ and $\text{Cs}_2\text{AgTlCl}_6$ are attractive for solar-cell absorbers as they have a small bandgap. In 2018, Karunadasa and co-workers first synthesized these two compounds through a modified slow cooling method.^[65] Both of them display a cubic double perovskite structure with $Fm\bar{3}m$ symmetry at room temperature. The CBM of $\text{Cs}_2\text{AgTlX}_6$ ($X = \text{Cl}$ and Br) contains mainly Tl-centered orbitals (with minor contributions from empty Ag 5s orbitals) while Ag-centered orbitals dominate the VBM, as shown in **Figure 7a**. Impressively, $\text{Cs}_2\text{AgTlCl}_6$ and $\text{Cs}_2\text{AgTlBr}_6$ have direct bandgaps of 2.0 and 0.95 eV, respectively, which are approximately 1 eV lower than those of analogous perovskites (such as $\text{Cs}_2\text{AgBiBr}_6$ and $\text{Cs}_2\text{AgBiCl}_6$) (**Figure 7b**). $\text{Cs}_2\text{AgTlBr}_6$ shows the lowest bandgap among all current halide perovskites. The decreased bandgaps of $\text{Cs}_2\text{AgTlBr}_6$ and $\text{Cs}_2\text{AgTlCl}_6$ can be attributed to two factors. First, a large overlap between the Tl^{3+} 6s (and some Ag^+ 5s) orbitals and halide orbitals results in a highly dispersive conduction band, and increasing bandwidth brings band extrema closer together. Second, the small bandgap is also related to the inherited small intrinsic energy difference between filled Ag 4d and vacant Tl 6s orbitals.^[65] Unfortunately, there is no PL in $\text{Cs}_2\text{AgTlBr}_6$ and $\text{Cs}_2\text{AgTlCl}_6$ even at 20 K, mainly because the symmetry-forbidden transition confined carriers to the forbidden region and prevented the radiative recombination. The excellent stability of $\text{Cs}_2\text{AgTlBr}_6$ and $\text{Cs}_2\text{AgTlCl}_6$ was proved by XRD patterns. They show no change upon exposure to light (0.75 sun at $\approx 60^\circ\text{C}$) or moist air (55% RH) over 40 days.^[65]

3.6. Au-Based HDPs

Another interesting group of HDPs is the mixed-valence perovskites in which B^+ and B^{3+} come from the same metal. A typical example is Au-based HDPs $\text{Cs}_2\text{Au}^+\text{Au}^{3+}\text{X}_6$ ($X = \text{Cl}^-$, Br^- and I^-), which were first synthesized by Guta in 1914.^[66] At room temperature, $\text{Cs}_2\text{Au}_2\text{X}_6$ crystallizes in a tetragonal structure with

space group $I4/mmm$, consisting of 3D metal halide frameworks formed by elongated $[\text{Au}^{3+}\text{X}_6]^{3-}$ octahedra and compressed $[\text{Au}^+\text{X}_6]^{5-}$ octahedra in a rocksalt ordering (**Figure 8a**).^[67] The CBM, taking Cs_2AuI_6 as an example, is mainly derived from the Au^{3+} $5d_{x^2-y^2}$ and I p orbitals and VBM consists mainly of the Au^+ $5d_z^2$ and I p orbitals (**Figure 8b**). The electronic band structure reveals that all these compounds have a slight indirect bandgap, where the VBM and CBM are at different points along the Γ to Σ' direction, and a direct bandgap appears at the high-symmetry N point, as shown in **Figure 8c**.^[68] It is worth noting that the difference between the indirect bandgap and optically allowed direct bandgap is tiny, only around 0.03 eV for $\text{Cs}_2\text{Au}_2\text{I}_6$. Attractively, the optical bandgap of $\text{Cs}_2\text{Au}_2\text{I}_6$ is around 1.06 eV,^[69] close to the ideal bandgap for single-junction solar cells as indicated by the Shockley–Queisser theory.^[70] The photo-conversion efficiency of $\text{Cs}_2\text{Au}_2\text{I}_6$ -based devices is predicted to be above 20%.^[71] $\text{Cs}_2\text{Au}_2\text{I}_6$ remains stable under ambient conditions for 40 days or heated below 140°C .^[69] Changing Cs^+ to a larger organic cation MA^+ , the crystal structure changed to a Ruddlesden–Popper (R–P)-type 2D structure.^[72] These 2D organic–inorganic gold HDPs $\text{MA}_2\text{Au}_2\text{X}_6$ also exhibit small bandgaps of 1.02 eV for $\text{MA}_2\text{Au}_2\text{I}_6$ crystals, 1.22 eV for $\text{MA}_2\text{Au}_2\text{I}_6$ films, and 1.38 eV for $\text{MA}_2\text{Au}_2\text{Br}_6$ films (**Figure 8d**).^[73]

4. HDPs Solar Cells

The report of $\text{Cs}_2\text{AgBiBr}_6$ in 2016 sparked great interest in HDPs. The first double perovskite solar cell devices were made in 2017 by Bein and co-workers, who solved the poor solubility of precursors by dissolving them in DMSO at 75°C , followed by spin coating for thin films.^[17] They emphasized that the high annealing temperature (250°C) is crucial for achieving a pure $\text{Cs}_2\text{AgBiBr}_6$ double perovskite phase. Furthermore, they developed the first $\text{Cs}_2\text{AgBiBr}_6$ solar cell device with the traditional mesoporous structure and achieved a PCE of 2.43% (**Figure 9a**).^[17] Impressively, these $\text{Cs}_2\text{AgBiBr}_6$ -based devices revealed excellent stability under permanent illumination for 100 mins or ambient conditions for at least 25 days. At the same

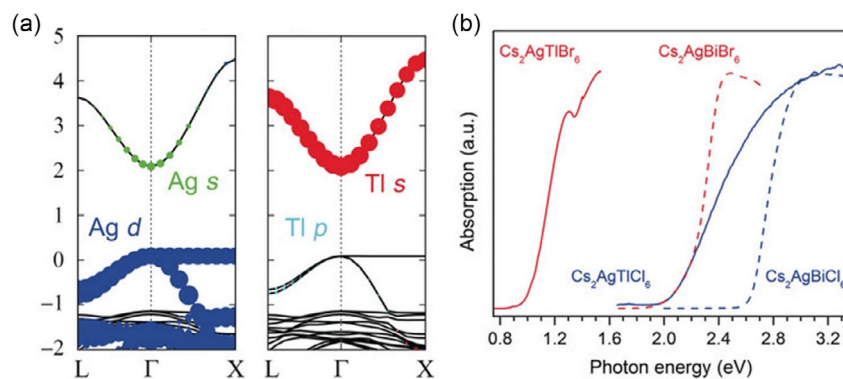


Figure 7. a) Band structures of $\text{Cs}_2\text{AgTlCl}_6$, calculated with DFT-HSE06 + SOC in their primitive unit cells using measured lattice parameters. Band structures are shown in duplicate with only metal orbital contributions shown; chloride orbitals are present but omitted for clarity. The conduction bands are rigidly shifted to match the experimental bandgaps, and all bands are shifted to align the Cs 5s bands. b) Absorption spectra of $\text{Cs}_2\text{AgTlBr}_6$ and $\text{Cs}_2\text{AgTlCl}_6$ (solid lines) and those of $\text{Cs}_2\text{AgBiBr}_6$ and $\text{Cs}_2\text{AgBiCl}_6$ (dashed lines). Reproduced with permission.^[65] Copyright 2018, Wiley-VCH.

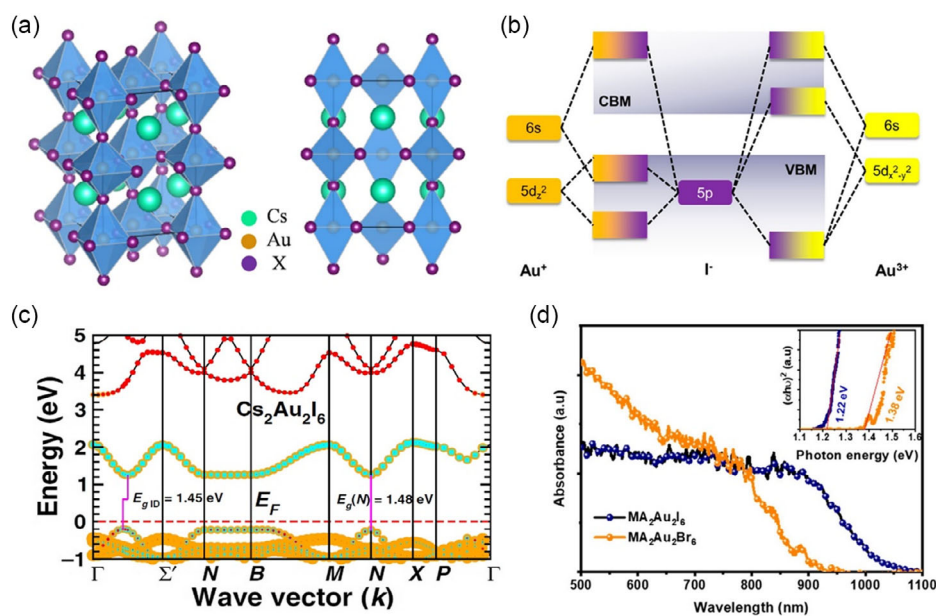


Figure 8. a) Schematic diagram of the structure of Cs₂Au₂X₆. Reproduced with permission.^[67] Copyright 2019, The Japan Society of Applied Physics. b) Molecular orbital diagram showing hybridizations in MA₂Au₂I₆ and Cs₂AuI₆. c) The Heyd-Scuseria-Ernzerhof (HSE06) electronic band structures of Cs₂Au₂X₆, X = I, Br, Cl, respectively, with the bandgap shifted to the HSE06-G0W0 calculated value. Orange, turquoise, and red symbols indicate 1 p, Au d, and Au s orbital character, respectively. (c) Reproduced with permission.^[68] Copyright 2020, American Physical Society. d) UV-vis absorption spectra of MA₂Au₂X₆ HDPs (inset: Tauc plot for MA₂Au₂X₆ to extract the direct bandgap). (b,d) Reproduced with permission.^[73] Copyright 2020, American Chemical Society.

time, we obtained a very uniform and high-quality Cs₂AgBiBr₆ thin film composed of single-layer nanocrystals by employing Cs₂AgBiBr₆ single crystals as the precursor solution. We further demonstrated the first planar Cs₂AgBiBr₆ solar cells with the structure of ITO/TiO₂/Cs₂AgBiBr₆ (205 nm)/Spiro-OMeTAD/Au. The champion device exhibits a power conversion efficiency (PCE) of 1.22 % with an open-circuit voltage (V_{oc}) of 1.06, a short-circuit current density (J_{sc}) of 1.55 mA cm⁻², and a fill factor (FF) of 74% (Figure 9b).^[48] There is almost no hysteresis for this planar device structure.

Up to now, various deposition methods have been employed to investigate the processes dependence on the PV performance of Cs₂AgBiBr₆ solar cells. The motivation to utilize different fabrication processes is to control the film crystallinity, morphology, orientation, thickness, phase purity, etc., which can influence the PCE of solar cell devices.^[74] Xiao and co-workers fabricated planar solar cells by low-pressure assisted solution processing under ambient conditions, and the optimized PCE is 1.44%.^[41] Liu and co-workers successfully prepared Cs₂AgBiBr₆ thin films through a sequential-vapor-deposition procedure. The device exhibited a PCE of 1.37% with V_{oc} of 1.12 V, J_{sc} of 1.79 mA cm⁻², and FF of 68% (Figure 9c).^[75] Meanwhile, they emphasize that excess BiBr₃ is critical to obtain stoichiometric Cs₂AgBiBr₆ double perovskite thin films. This was further confirmed by Yang and co-workers. They also noticed that the vapor-processed film exhibits a deviating composition stoichiometry due to a larger loss of Br.^[76] The vapor-processed devices retained over 90% of their initial PCEs after being kept in ambient without encapsulation for 350 h. The antisolvent dropping method, a widely used approach in Pb-based perovskite solar cells, was also applied to deposit

Cs₂AgBiBr₆ thin films with ultrasmooth morphology, micro-sized grains, and high crystallinity. The resulting solar cells show an optimized PCE of 2.23% with V_{oc} = 1.01 V, J_{sc} = 3.19 mA cm⁻², and FF = 69.2%.^[77] Besides, these devices hold 90% of their origin PCEs after 10 days of storage and show negligible performance decrease during annealing at 100 °C for 60 mins.

An interesting strategy to increase the J_{sc} of Cs₂AgBiBr₆ solar cells is to employ a dye-sensitized electron transport layer (ETL) or hole-transporting layer (HTL). For example, the device based on C-Chl-sensitized mesoporous TiO₂ can increase the J_{sc} from 3.22 to 4.09 mA cm⁻², thus pushing the PCE to 3.11%.^[78] Similarly, by employing D149 indoline to sensitize the TiO₂ ETL and introducing Ti₃C₂T_x MXene nanosheets into Cs₂AgBiBr₆, the J_{sc} of the resulting device reached up to 8.85 mA cm⁻² (Figure 9d). The external quantum efficiency (EQE) spectra confirm that the improved photocurrent mainly comes from the dyes' additional sunlight absorption between 500 and 650 nm (Figure 9e). As a result, a very high PCE of 4.47% was achieved.^[79] Moreover, the D149-Cs₂AgBiBr₆@Ti₃C₂T_x-based devices show enhanced long-term stability with only 14% PCE losses after 1000 h of storage in air (about 20% relative humidity) without encapsulation. Except for modifying ETL, a photoactive dye Zn-Chl as an HTL was utilized in Cs₂AgBiBr₆ devices. As shown in Figure 9f, the Zn-Chl-sensitized solar cell exhibits a PCE of 2.79%, with a J_{sc} of 3.83 mA cm⁻², which is 22–27% higher than the devices with conventional hole transport materials (HTMs) such as Spiro-OmeTAD, P3HT and PTAA.^[80] Although this strategy achieved relatively high J_{sc} and PCEs, the improvement mainly comes from the contribution of dyes rather than the Cs₂AgBiBr₆ absorber.

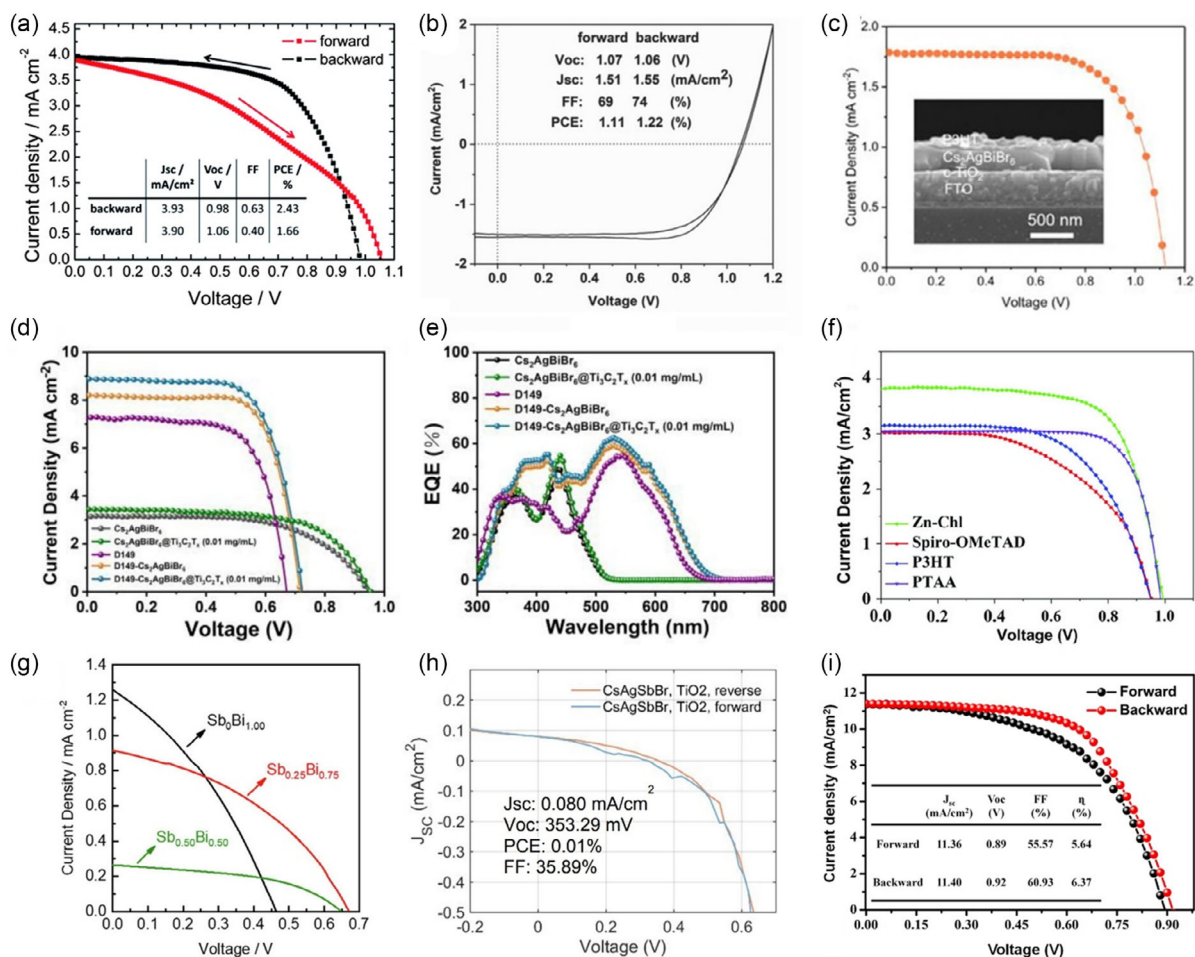


Figure 9. J - V curve of the optimized $\text{Cs}_2\text{AgBiBr}_6$ devices with a) mesoporous structure and b) planar structure. (a) Reproduced with permission.^[17] Copyright 2017, Royal Society of Chemistry. (b) Reproduced with permission.^[48] Copyright 2018, Wiley-VCH. (c) J - V curve of the optimized solar cell fabricated by sequential vapor deposition. Inset: cross-sectional SEM image of the device. Reproduced with permission.^[75] Copyright 2018, Wiley-VCH. (d) J - V curves of devices on the basis of $\text{Cs}_2\text{AgBiBr}_6$ with or without D149-sensitized TiO_2 and/or $\text{Ti}_3\text{C}_2\text{T}_x$ doping. Reproduced with permission.^[79] Copyright 2022, Elsevier B.V. (e) Their corresponding EQE spectra. Reproduced with permission.^[79] Copyright 2022, Elsevier B.V. (f) Typical J - V curves of $\text{Cs}_2\text{AgBiBr}_6$ solar cells with various HTMs. (2,2',7,7'-tetrakis(*N,N*-di-*p*-methoxyphenylamine)-9,9'-spirobifluorene (Spiro-OMeTAD), poly(3-hexylthiophene) (P3HT), and poly(triarylamine) (PTAA)). Reproduced with permission.^[80] Copyright 2020, Wiley-VCH. (g) Representative J - V curves of the $\text{Cs}_2\text{AgSb}_x\text{Bi}_{(1-x)}\text{Br}_6$ ($x = 0, 0.25, 0.50$) double-perovskite solar cells. Reproduced with permission.^[81] Copyright 2019, Elsevier Ltd. (h) J - V curve of $\text{Cs}_2\text{AgSbBr}_6$ solar cells. Reproduced with permission.^[53] Copyright 2019, Royal Society of Chemistry. (i) J - V curves under reverse and forward bias of 1200 s hydrogenated $\text{Cs}_2\text{AgBiBr}_6$ solar cells. Reproduced with permission under the terms of the Creative Commons CC BY license.^[21] Copyright 2022, the Author. Published by Springer Nature.

Element doping/alloying is an efficient strategy to expand the intrinsic absorption properties of $\text{Cs}_2\text{AgBiBr}_6$. By replacing Bi^{3+} with Sb^{3+} in the structure, a series of $\text{Cs}_2\text{AgSb}_x\text{Bi}_{(1-x)}\text{Br}_6$ ($x = 0, 0.25, 0.50, 0.75$) thin films with gradually decreased bandgap was achieved. The fabricated solar cell using the $\text{Cs}_2\text{AgSb}_{0.25}\text{Bi}_{0.75}\text{Br}_6$ thin film show an obvious PCE improvement over the reference $\text{Cs}_2\text{AgBiBr}_6$ solar cell, as shown in Figure 9g.^[81] However, the J_{sc} was not increased as expected, but decreased after Sb^{3+} alloying, possibly due to the presence of large pinholes. By totally replacing Bi^{3+} with Sb^{3+} , another novel $\text{Cs}_2\text{AgSbBr}_6$ HDP can be formed. Due to the existence of the impurity phases as discussed above, the $\text{Cs}_2\text{AgSbBr}_6$ -based solar cells only yield a very low PCE of 0.01% with $V_{oc} = 0.35$ V, $J_{sc} = 0.08$ mA/cm^2 , and FF = 35.9% (Figure 9h).^[53] Quite

recently, a novel hydrogen atom interstitial doping could significantly decrease the bandgap of $\text{Cs}_2\text{AgBiBr}_6$ film from 2.18 to 1.64 eV. Impressively, the J_{sc} of the solar cell increases dramatically from 1.03 to 11.4 mA/cm^2 with record PCE values of 5.64% and 6.37% for forward and backward scans, respectively (Figure 9i).^[21] Meanwhile, these hydrogenated $\text{Cs}_2\text{AgBiBr}_6$ solar cells exhibit excellent stability; they maintained nearly 95%, 91%, and 84% of initial PCE after being treated in nitrogen at 20 °C with light illumination and 85 °C without or with light illumination for 1440 h, respectively. However, besides $\text{Cs}_2\text{AgBiBr}_6$, the mixed-valence HDP MA_2AuBr_6 has recently been used as an absorber; however, the device shows a very poor PCE of 0.007%.^[73] Table 2 summarizes the device architecture and photovoltaic parameters of HDP-based solar cells.

Table 2. Device architecture and photovoltaic parameters of HDP-based solar cells.

| Device configuration | Fabrication method | V_{oc} [V] | J_{sc} [mA cm^{-2}] | FF | PCE [%] | References |
|--|--|--------------|----------------------------------|-------|---------|------------|
| FTO/c-TiO ₂ /m-TiO ₂ /Cs ₂ AgBiBr ₆ /Spiro-OMeTAD/Au | One-step spin coating | 0.98 | 3.93 | 0.63 | 2.43 | [17] |
| ITO/c-TiO ₂ /Cs ₂ AgBiBr ₆ /Spiro-OMeTAD/Au | One-step spin coating | 1.06 | 1.55 | 0.74 | 1.22 | [48] |
| ITO/SnO ₂ /Cs ₂ AgBiBr ₆ /P3HT/Au | One-step spin coating and low-pressure-assisted method | 1.04 | 1.78 | 0.78 | 1.44 | [41] |
| FTO/c-TiO ₂ /Cs ₂ AgBiBr ₆ /P3HT/Au | Sequential vapor deposition | 1.12 | 1.79 | 0.68 | 1.37 | [75] |
| ITO/c-TiO ₂ /Cs ₂ AgBiBr ₆ /Spiro-OMeTAD/MoO ₃ /Au | Sequential vapor deposition | 1.05 | 2.06 | 0.65 | 1.41 | [76] |
| ITO/c-TiO ₂ /Cs ₂ AgBiBr ₆ /Spiro-OMeTAD/MoO ₃ /Au | One-step spin coating | 1.01 | 3.82 | 0.65 | 2.51 | [76] |
| ITO/Cu–NiO/Cs ₂ AgBiBr ₆ /C60/BCP/Ag | One-step spin coating with antisolvent | 1.01 | 3.19 | 0.69 | 2.23 | [77] |
| FTO/c-TiO ₂ /C–chl m-TiO ₂ /Cs ₂ AgBiBr ₆ /Spiro-OMeTAD/Ag | One-step spin coating | 1.04 | 4.09 | 0.73 | 3.11 | [78] |
| FTO/c-TiO ₂ /m-TiO ₂ /D149/Cs ₂ AgBiBr ₆ -Ti ₃ C ₂ T _x /Spiro-OMeTAD/Ag | One-step spin coating | 0.722 | 8.85 | 0.701 | 4.47 | [79] |
| ITO/SnO ₂ /Cs ₂ AgBiBr ₆ /Zn–chl/Ag | One-step spin coating | 0.99 | 3.83 | 0.736 | 2.79 | [80] |
| FTO/c-TiO ₂ /m-TiO ₂ /Cs ₂ AgSb _{0.25} Bi _{0.75} Br ₆ /Spiro-OMeTAD/Au | Dip coating | 0.64 | 1.03 | 0.38 | 0.25 | [81] |
| FTO/c-TiO ₂ /Cs ₂ AgSbBr ₆ /Spiro-OMeTAD/Au | One-step spin coating | 0.35 | 0.08 | 0.359 | 0.01 | [53] |
| FTO/c-TiO ₂ /m-TiO ₂ /Cs ₂ AgBiBr ₆ /PTB7/Au | One-step spin coating | 0.95 | 3.5 | 0.76 | 2.53 | [106] |
| FTO/c-TiO ₂ /Cs ₂ AgBiBr ₆ /PBDB-T /MoO ₃ /Ag | One-step spin coating with antisolvent | 1.278 | 3.34 | 0.775 | 3.31 | [108] |
| ITO/SnO ₂ / hydrogenated Cs ₂ AgBiBr ₆ /Spiro-OMeTAD/Au | One-step spin coating with antisolvent | 0.92 | 11.4 | 0.609 | 6.37 | [21] |
| FTO/m-TiO ₂ /MA ₂ AuBr ₆ /PTAA/Au | Reactive polyiodide melt | 0.33 | 0.052 | 0.410 | 0.007 | [73] |

5. Challenges and Efforts in HDPs Solar Cells

Although intensive efforts have been devoted to HDPs solar cells, especially Cs₂AgBiBr₆ devices, the highest reported PCE of 6.37% is still far from the expectation. Moreover, except for Cs₂AgBiBr₆, Cs₂AgSb_xBi_(1-x)Br₆, and MA₂AuBr₆, it has not been possible to employ other HDPs in solar cells so far. Understanding and addressing the challenges which hinder HDPs are crucial for achieving high-efficiency devices. In this section, we summarize these major challenges from two perspectives, material intrinsic properties and device fabrication, including large bandgap, indirect bandgap nature, parity-forbidden transitions, low electronic dimensionality, weak or no PL, difficulties to fabricate and dope/alloy HDP films, contacts issues, short carrier diffusion length, and high defect density in thin films. Along with the challenges, we also highlight the recent efforts, possible solutions, and our views.

5.1. Large Bandgap

The Shockley–Queisser limit indicates that the best bandgap for single-junction solar cells is around 1.1 to 1.4 eV.^[70] Unfortunately, most report HDPs show very large bandgaps above 2 eV (Figure 10a). One reason is that most of these stable HDPs are Cl-based compounds, usually exhibiting relatively large bandgaps compared to I[−] and Br[−]-based analogues. Changing the halide or halide mixing is a simple yet efficient method because the states of halogen orbitals dominate their VBM. As discussed in Section 2, almost no I-based and only a few Br-based HDPs can be successfully synthesized, mainly due to the smaller octahedral factor μ ($\mu < 0.41$) and thermodynamic instability. Another popular strategy of decreasing the bandgap by halide mixing cannot always work well in HDPs.

Take Bi-based HDPs as an example; only a low level (<3 mol%) of I[−] can be doped into the Cs₂AgBiBr₆ and Cs₂AgBiCl₆ host lattices. Further increasing I[−] will lead to phase segregation of Ag- and Bi-rich nonperovskite compounds (Figure 10b).^[82] An exceptional finding is that the Cs₂AgBiI₆ nanocrystals synthesized by the anion exchange method could be stable for a short time.^[51] Actually, there are also some HDPs with low bandgaps, including Cs₂Au₂I₆ (1.06, 1.31 eV),^[69,83] MA₂Au₂I₆ (1.02, 1.22 eV),^[72,73] MA₂Au₂Br₆ (1.38 eV),^[73] Cs₂AgSbBr₆ (1.64 eV),^[53] Cs₂AgFeCl₆ (1.62 eV),^[64] and Cs₂AgTlBr₆ (0.95 eV)^[65]; however, all these materials have not yet been successfully used in efficient solar cell devices due to other challenges, which will be discussed later.

Metal doping/alloying is a general approach to modifying the bandgap of semiconductors. In HDPs, two different B-site metal ions provide more degrees of freedom in selecting the suitable dopants, including isovalent (monovalent and trivalent) and heterovalent (bivalent and tetravalent) metal doping/alloying.^[84] Toxic Tl³⁺ was the first reported ion to dope Cs₂AgBiBr₆ to reduce the bandgap by 0.8 eV.^[85] Mitzi and co-workers employed Sb³⁺ and In³⁺ to tune the bandgap of Cs₂AgBiBr₆, where Sb³⁺ doping decreased the bandgap to 1.86 eV, but In³⁺ doping increased the bandgap to 2.27 eV.^[44] The bandgap of HDP Cs₂NaFeCl₆ was also significantly decreased from 2.06 eV to approximately 1.62 eV by partial/complete substitution of monovalent Na⁺ with Ag⁺ (Figure 11a).^[30] Similarly, we have successfully alloyed Fe³⁺ into Cs₂AgInCl₆, tuning the bandgap of Cs₂AgIn_{1-x}Fe_xCl₆ ($x = 0-1$) from 2.8 to 1.6 eV (Figure 11b).^[64] Apart from isovalent doping/alloying, heterovalent doping has also been investigated. As shown in Figure 11c, Sn²⁺/Sn⁴⁺ can be doped in Cs₂AgBiBr₆ with a bandgap reduction of up to 0.5 eV.^[86] Another example is Cu²⁺-doped Cs₂AgSbCl₆, which reduced the bandgap from 2.6 to 1 eV.^[87] As mentioned above,

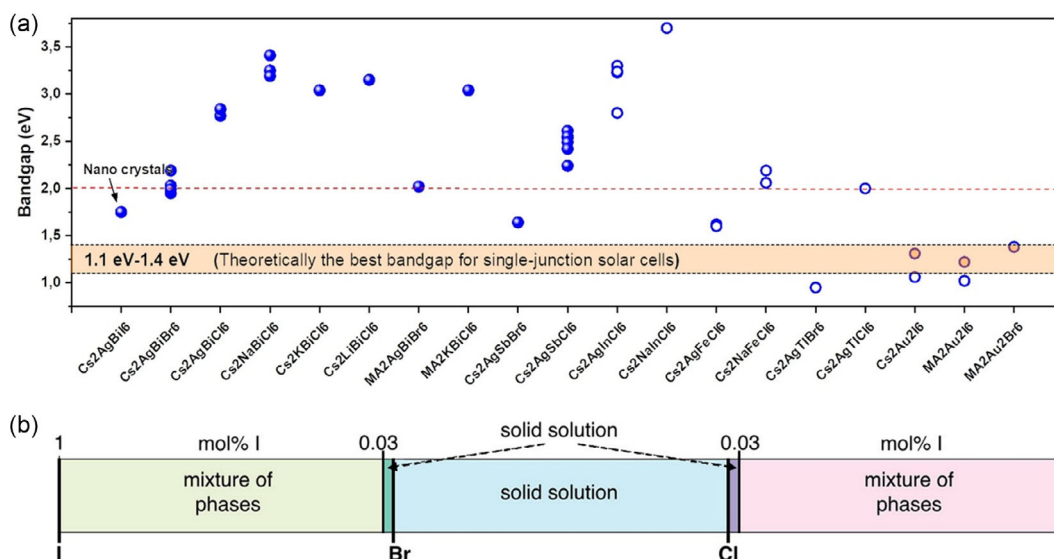


Figure 10. a) Optical bandgaps of various HDPs. Different bandgap values in the same compound could be related to different measurement methods and/or different sample forms (crystals or powders or films). The blue spheres and circles represent indirect and direct bandgap, respectively. b) Schematic representation of the $\text{Cs}_2\text{AgBiX}_6$ ($X = \text{Cl}/\text{Br}$, Br/I and Cl/I) miscibility. Reproduced with permission under the terms of the Creative Commons CC BY license.^[82] Copyright 2020, the Author. Published by American Chemical Society.

Sui and co-workers recently demonstrated that atomic hydrogen could be doped into interstitial sites of $\text{Cs}_2\text{AgBiBr}_6$ lattice and reduce the $\text{Cs}_2\text{AgBiBr}_6$ film's bandgap from 2.18 to 1.64 eV (Figure 10d).^[21] Instead of decreasing the bandgap, some dopants could introduce a new sub-bandgap inside the pristine bandgap of HDPs with strong absorption in NIR light (Figure 11e). For example, we successfully introduce a sub-bandgap in the $\text{Cs}_2\text{AgBiBr}_6$ system through $\text{Cu}^+/\text{Cu}^{2+}$ doping for the first time, expanding its absorption edge to approximately 860 nm (Figure 11f).^[88] A similar phenomenon was observed in Fe^{2+} and Ru^{3+} alloyed $\text{Cs}_2\text{AgBiBr}_6$ single crystals; the absorption range significantly broadened to 1350 nm and 1200 nm, respectively.^[89,90] These HDPs with sub-bandgap are promising for intermediate band solar cells, which could surpass the Shockley–Queisser efficiency limit to obtain an efficiency of 63% theoretically.^[91]

It has been well known that changing the atomic arrangement can effectively modify the band structure of semiconductors.^[92,93] As expected, changing the Ag–Bi order to disorder in $\text{Cs}_2\text{AgBiBr}_6$ can also engineer its band structure, as evidenced by the first-principle results.^[94] In HDPs, the ordered structure corresponds to the alternating arrangement of B^+ and B^{3+} cations in the lattice, while disorder structure means that some B^+ and B^{3+} ions randomly occupy the B site. As shown in Figure 11g, the calculated bandgap of ordered $\text{Cs}_2\text{AgBiBr}_6$ is 1.93 eV, which is quite close to the experimental result. Partially changing the Ag and Bi arrangement can significantly decrease the bandgap to 1.46 eV. Further increasing the degree of disorder to a fully disordered structure, a small bandgap of 0.44 eV could be achieved.^[94] These have also been verified by experimental results. We obtained black $\text{Cs}_2\text{AgBiBr}_6$ single crystals with a small bandgap of 1.72 eV by simply changing the crystal growth temperature from 60 °C to 150 °C (Figure 11h).^[39]

Later, Huang and co-workers observed that simply postannealing a $\text{Cs}_2\text{AgBiBr}_6$ crystal at 400 °C for 24 h could decrease the bandgap to around 1.69 eV (Figure 11i).^[40] These results imply the thermal energy may be the driving force to overcome the order-to-disorder transition barrier to achieve partially disordered $\text{Cs}_2\text{AgBiBr}_6$ crystals. It is noted that a direct evidence of atomic rearrangement is still missing. Currently, a simple way to qualitative the degree of disorder in $\text{Cs}_2\text{AgBiBr}_6$ is by evaluating the diffraction intensity ratio of the (111) and (022) planes (I_{111}/I_{022}), where a higher ratio represents better B-site cation ordering based on the extinction law.^[95]

The bandgap of HDPs can also be tuned by some physical posttreatment, such as high-pressure and high-temperature treatment. Under high pressure at a 15 GPa, the bandgap of benchmark $\text{Cs}_2\text{AgBiBr}_6$ was reduced from 2.2 eV to around 1.7 eV, which could be explained by the phase transition and subsequent structural amorphization of tetragonal $\text{Cs}_2\text{AgBiBr}_6$ at high pressure.^[96] Unfortunately, only around 8.2% of bandgap narrowing can be retained after releasing pressure. Regarding high-temperature treatment, a fully reversible thermochromism was observed in $\text{Cs}_2\text{AgBiBr}_6$ crystals and thin films between room temperature and 250 °C.^[97]

5.2. Indirect Bandgap Nature

Besides large bandgap values, the indirect bandgap property of some HDPs usually causes a low absorption coefficient due to the phonon-assisted processes. In semiconductor physics, the direct and indirect bandgap can be characterized by a certain crystal momentum (k -vector) in the Brillouin zone of the CBM and VBM. The location of CBM and VBM in band structure at the same K -vector would induce the direct bandgap (Figure 12a). The indirect bandgap refers to the band structure

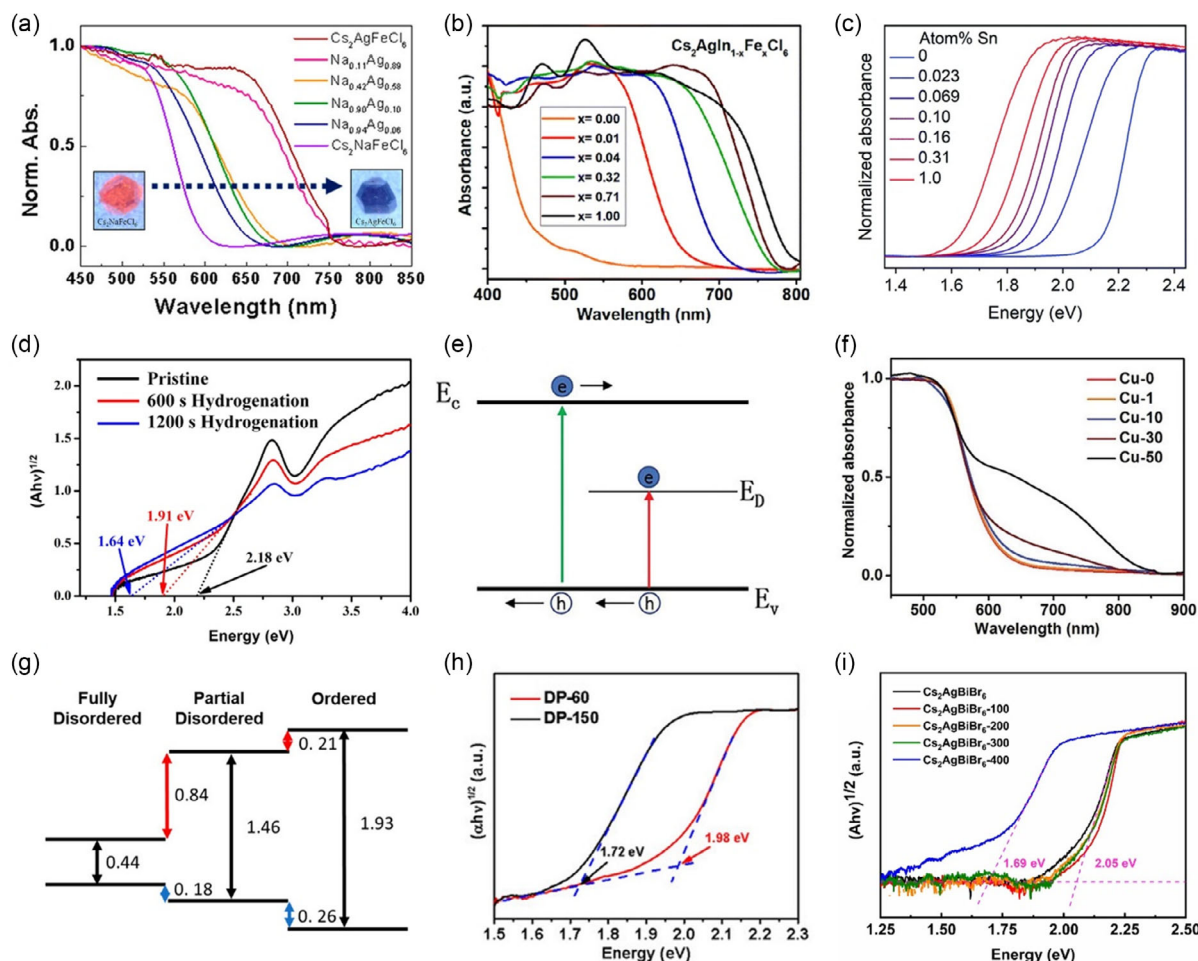


Figure 11. a) UV–vis spectra of the $\text{Cs}_2\text{Ag}_x\text{Na}_{1-x}\text{FeCl}_6$ ($x = 0, 0.06, 0.10, 0.58, 0.89, 1$) single crystals. The inset shows the optical images of $\text{Cs}_2\text{NaFeCl}_6$ and $\text{Cs}_2\text{AgFeCl}_6$. Reproduced with permission.^[30] Copyright 2020, American Chemical Society. b) Normalized UV–vis absorption spectra of $\text{Cs}_2\text{AgIn}_{1-x}\text{Fe}_x\text{Cl}_6$ ($x = 0.00, 0.01, 0.04, 0.32, 0.71, \text{ and } 1.00$) crystals. Reproduced with permission under the terms of the Creative Commons CC BY license.^[64] Copyright 2021, the Author. Published by the Royal Society of Chemistry. c) UV–vis absorbance spectra of crystals of $\text{Cs}_2\text{AgBiBr}_6$ and Sn-alloyed $\text{Cs}_2\text{AgBiBr}_6$ converted from diffuse reflectance spectra using the Kubelka–Munk transformation. Reproduced with permission under the terms of the Creative Commons CC BY license.^[86] Copyright 2019, the Authors. Published by the Royal Society of Chemistry. d) Tauc plots of the $\text{Cs}_2\text{AgBiBr}_6$ perovskite films with different hydrogenation time, which is calculated through the indirect bandgap method. Reproduced with permission under the terms of the Creative Commons CC BY license.^[21] Copyright 2022, the Author. Published by Springer Nature. e) Schematic illustration of the typical interband transition and the defect-to-band transition. f) Normalized UV–vis absorption of pristine $\text{Cs}_2\text{AgBiBr}_6$ (Cu-0) and $\text{Cs}_2(\text{Ag}:\text{Cu})\text{BiBr}_6$ (Cu-1, Cu-10, Cu-30, Cu-50) double perovskites. Reproduced with permission.^[88] Copyright 2020, the Authors. Published by Wiley-VCH. g) Band alignment of the ordered, partial disordered, and fully disordered $\text{Cs}_2\text{AgBiBr}_6$. Reproduced with permission.^[94] Copyright 2018, American Chemical Society. h) Tauc plots of DP-60 and DP-150 for indirect bandgap semiconductor. DP-60 and DP-150 correspond to $\text{Cs}_2\text{AgBiBr}_6$ crystals obtained by evaporation at 60 and 150 °C, respectively. Reproduced with permission under the terms of the Creative Commons CC BY license.^[39] Copyright 2020, the Authors. Published by Wiley-VCH. i) Tauc plots of the pristine $\text{Cs}_2\text{AgBiBr}_6$ single crystal and those annealed at different temperatures. Reproduced with permission.^[40] Copyright 2022, Wiley-VCH.

of CBM and VBM with different \mathbf{K} vectors, as shown in Figure 12b. Light absorption easily happens at direct bandgap materials due to the conserved momentum. However, this process is difficult in indirect bandgap materials, which require the emission or absorption of a phonon to conserve momentum. As a result, the light absorption in indirect bandgap materials is less efficient with a lower absorption coefficient than those in direct bandgap materials. This can explain why $\text{Cs}_2\text{AgBiBr}_6$ thin films show very poor absorbance in the range of 500–600 nm, as discussed previously in Figure 3d. Besides $\text{Cs}_2\text{AgBiBr}_6$, many

HDPs exhibit an indirect bandgap (Figure 10a, blue spheres), hindering them from being effective solar absorbers.

Normally, it is difficult to independently adjust the CBM and VBM because they are typically paired bonding and antibonding states, respectively. Interestingly, it is possible to independently modify them in HDPs because the CBM and VBM could separately derive from two different B-site cations. For instance, along with increasing the In^{3+} composition to replace Sb^{3+} in $\text{Cs}_2\text{AgSbCl}_6$, the character of CBM was gradually changed from $\text{Sb} 5p$ -derived to $\text{In} 5s$ -derived, as shown in Figure 12c.^[55] After more than

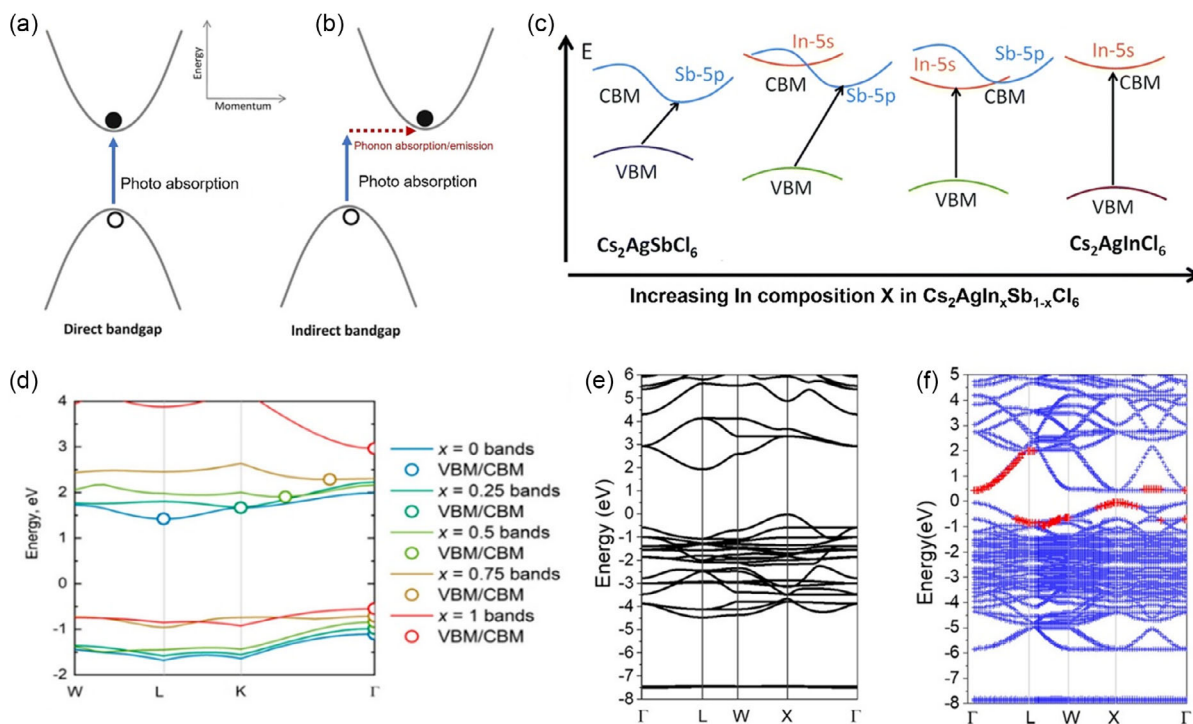


Figure 12. Photon absorption process in a) the direct and b) the indirect bandgap semiconductors. c) The schematic representation of the proposed band diagram of $\text{Cs}_2\text{AgIn}_x\text{Sb}_{1-x}\text{Cl}_6$. Reproduced with permission.^[53] Copyright 2017, Royal Society of Chemistry. d) Indirect to direct bandgap transition of $\text{Cs}_2\text{Bi}_{1-x}\text{In}_x\text{AgCl}_6$ by using the calculated electronic band structure. Reproduced with permission.^[98] Copyright 2020, American Chemical Society. Corresponding band structure of e) the ordered $\text{Cs}_2\text{AgBiBr}_6$ and f) fully disordered $\text{Cs}_2\text{AgBiBr}_6$ in the primitive Brillouin Zone. The red dots in (b) represent the dots at the band edge with the spectral weight over 50%. Reproduced with permission.^[94] Copyright 2018, American Chemical Society.

40% In^{3+} alloyed in the host structure, the bandgap of alloys changed from indirect to direct property. A similar phenomenon occurred in In^{3+} alloyed $\text{Cs}_2\text{AgBiCl}_6$ by adjusting the K-vector of CBM from the L point to the Γ point, as shown in Figure 12d.^[98]

Apart from changing the composition, the band characteristics in HDPs could also be modified by the order to disorder transition of the B-site cation.^[94] Figure 12e shows the band structure of the ordered $\text{Cs}_2\text{AgBiBr}_6$ with the typical indirect bandgap nature, while the band structure of the fully disordered $\text{Cs}_2\text{AgBiBr}_6$ is quite different from the ordered one. Not only the bandgap value was reduced to 0.44 eV, but also the band features were changed (Figure 12f). In the disordered $\text{Cs}_2\text{AgBiBr}_6$, a significant amount of pseudo-direct bandgap components appeared.

5.3. Parity-Forbidden Transitions

Another challenge for In- and Tl-based HDPs with direct bandgaps is the parity-forbidden transitions. Light absorption in centrosymmetric solids follows the Laporte selection rule, where the optical transitions between two identical inversion symmetry states are parity-forbidden (also called symmetry-forbidden).^[59] The parity-forbidden transitions lead to weak absorption of photons with energies close to the bandgap, undesirable for thin-film absorber applications (Figure 13a). Taking $\text{Cs}_2\text{AgTlCl}_6$ as an example, both the A_{1g} orbital in the CBM and E_g orbital in the VBM have the same gerade symmetry; a parity-forbidden transition occurs (Figure 13b).^[99] The optical transitions

gradually become allowed as the k point changes from Γ to L point because ungerade symmetry is introduced to the electronic states, which is evident in the calculated dipole transition matrix element, as shown in Figure 13c,d.^[65,99] The parity-forbidden transition at the Γ point was also observed in $\text{Cs}_2\text{AgInCl}_6$, where the transition has been assigned as $E_g (\Gamma_3^+)$ to $A_{1g} (\Gamma_1^+)$ (Figure 5a).^[59]

A common approach to break the parity-forbidden transition is metal doping/alloying at sufficiently high levels. The requirement for the dopants is a distinctively different electronic configuration from the substituted cation in the structure. For example, in Na^+ alloyed/doped $\text{Cs}_2\text{AgInCl}_6$, Na^+ can efficiently break the parity-forbidden transition of the host material.^[100] Similarly, Bi^{3+} can change the symmetry and bandgap nature of $\text{Cs}_2\text{AgTlCl}_6$ after replacing enough Tl^{3+} .^[99] Notably, the narrow forbidden region would not reduce the light absorption substantially if allowed transitions close to the band edge. Instead, the narrow forbidden region could act as carriers funnel and slow carrier recombination, which are advantageous for solar absorbers.^[99] The region of the symmetry-forbidden transitions in $\text{Cs}_2\text{AgTlCl}_6$ is small with a value of 0.17 eV above the band edge (Figure 13e).^[65] This region in $\text{Cs}_2\text{AgInCl}_6$ is 0.27 eV.^[65]

5.4. Low Electronic Dimensionality

Electronic dimensionality describes the connectivity of the atomic orbitals that comprise the lower conduction band

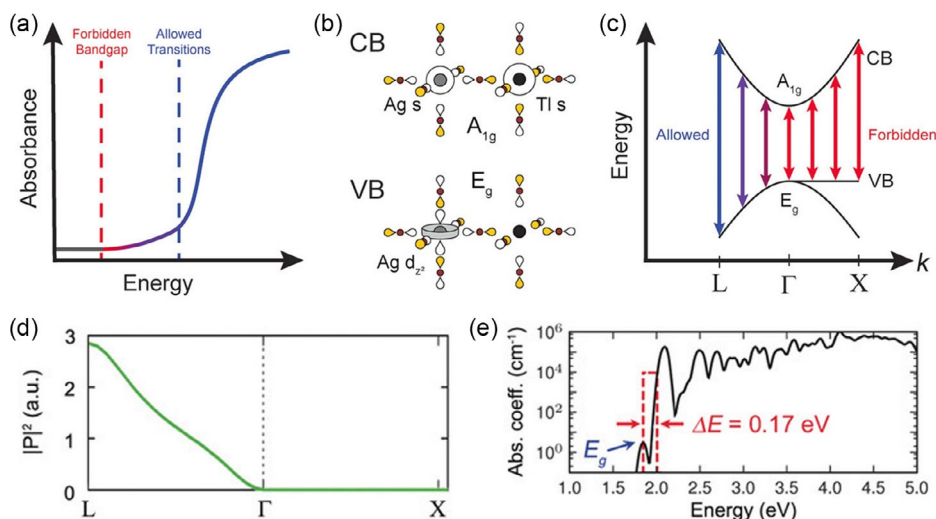


Figure 13. Schematic illustration of symmetry-forbidden bandgaps using $\text{Cs}_2\text{AgTlCl}_6$ as an example. a) The weak absorption onset expected for a material with a symmetry-forbidden bandgap. b) Schematic orbital representation of the valence band (VB) and conduction band (CB) at G in $\text{Cs}_2\text{AgTlCl}_6$. The VB contains Cl p and Ag d orbitals, whereas the CB contains Cl p , Ag s , and Tl s orbitals. c) Band diagram depicting allowed and forbidden optical transitions in $\text{Cs}_2\text{AgTlCl}_6$. At G, the bandgap transition is forbidden because of the shared gerade symmetry of the VB and CB. Transitions become allowed on moving from G to L because ungerade character is introduced. Reproduced with permission.^[99] Copyright 2021, Wiley-VCH. d) Transition dipole matrix elements ($|P|^2$) along high-symmetry lines in reciprocal space calculated within the independent particle approximation. e) Absorption spectrum of $\text{Cs}_2\text{AgTlCl}_6$ calculated using the ab initio GW-Bethe-Salpeter approach. The red box highlights the symmetry-forbidden region. Reproduced with permission.^[65] Copyright 2018, Wiley-VCH.

(LCB) and upper valence band (UVB).^[101] Usually, perovskite materials with high structure dimensionality, such as Pb-based perovskites, show high electronic dimensionality. However, most HPDs with 3D crystal structures exhibit lower dimensional electronic structures (0D or quasi-0D), resulting in large carrier effective masses, isotropic current flow, and fundamentally deeper defect states. The reason is mainly due to their typical rock-salt ordered crystal structure (Figure 14b). That is, alternating $[\text{B}^+\text{X}_6]^{5-}$ and $[\text{B}^{3+}\text{X}_6]^{3-}$ octahedra lead to the 0D connectivity

of the same octahedra. Taking $\text{Cs}_2\text{AgBiBr}_6$ as an example, the CBM is mainly derived from Bi $6p$ states, whereas the VBM is primarily derived from Ag $4d$ -Br $5p$ antibonding states, as we discussed in Figure 3a,b. As the Bi $6s$ orbitals do not contribute to the VBM, the VBM-deriving Ag $4d$ and Br $5p$ orbitals cannot connect 3-dimensionally due to the isolated $[\text{AgBr}_6]^{5-}$ octahedra in the framework, making $\text{Cs}_2\text{AgBiBr}_6$ a 0D electronic dimensionality. Correspondingly, choosing appropriate B-site cations and B-site alloying is possible to change the electronic

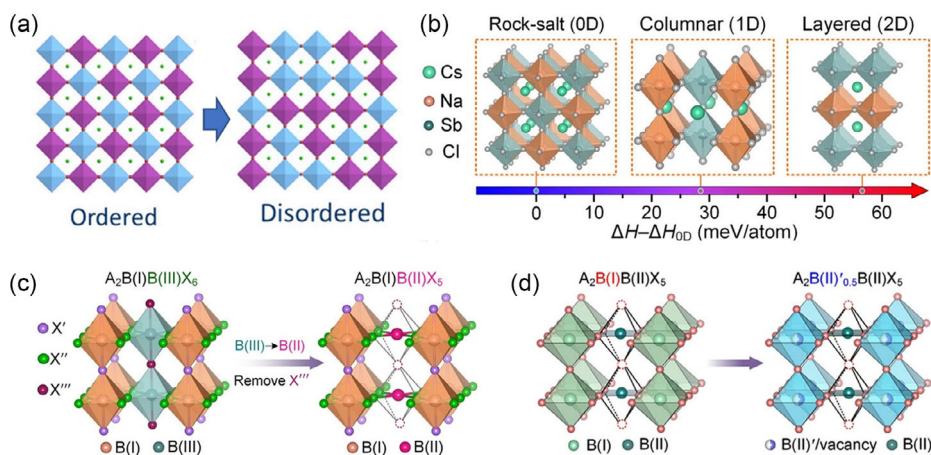


Figure 14. a) Schematic illustration of the ordered and disordered structures of HPDs. The disordered structure just gives one possible case. Reproduced with permission.^[94] Copyright 2018, American Chemical Society. b) Calculated formation enthalpies of $\text{Cs}_2\text{NaSbCl}_6$ with columnar-ordered (1D) and layered-ordered (2D) arrangements, with respect to that with the rock-salt-ordered (0D) arrangement. c) Structural evolution from columnar-ordered $\text{A}_2\text{B}^+\text{B}^{3+}\text{X}_6$ to columnar-ordered $\text{A}_2\text{B}(\text{B}(\text{II}))\text{X}_5$ via removing the halogen anions between the B^{2+} cations to keep the charge balance. Reproduced with permission.^[15] Copyright 2021, American Chemical Society. d) Structural evolution from $\text{A}_2\text{B}^+\text{B}^{2+}\text{X}_5$ to $\text{A}_2\text{B}^{2+/0.5}\text{B}^{2+}\text{X}_5$ HPDs via replacing every two B^+ cations by one B^{2+} cation and one vacancy. Reproduced with permission.^[103] Copyright 2021, American Chemical Society.

properties. It has been predicted that the In^-/Tl^- and Bi/Sb -based HDPs show electrical 3D structures, as both In^- and Tl^- have a similar contribution to the LCB and UVB.^[56,59,102] However, besides the toxicity of Tl , Tl^-/In^- would be easily oxidized to $\text{Tl}^{3+}/\text{In}^{3+}$, making it challenging to synthesize related compounds. So, it is still highly desirable to develop alternative suitable B-site cation alloyed or new HDPs.

Besides composition engineering, changing the B-site cations arrangement is another straightforward approach to alter the electronic properties of HDPs. In other words, the electronic dimensionality can be increased by destroying the typical rock-salt ordered structure to make the same octahedra connection. This can be achieved by the order-to-disorder transition of the B-site cations arrangement, as we mentioned previously (Figure 14a).^[94] Compared to random and partial change, it is more attractive if these B-site cations can be arranged in a controlled way. Xiao and co-workers theoretically demonstrated two HDP structures with columnar (1D) and layered (2D) B-site orderings, as shown in Figure 14b, which could increase the electronic dimensionality from 0D to 1D and 2D, respectively.^[15] Unfortunately, due to the large charge difference between two different B-site cations, B^+ and B^{3+} , these two structures have larger formation enthalpies than the ordered structure, indicating that both cannot be synthesized experimentally. Along this line, reducing the charge difference could help stabilize the columnar and even layered B-site ordered structure. This idea has been proved by substituting the B^{3+} cations with B^{2+} decreased the B-site charge difference from 2 to 1 to form the columnar B-site ordered structure with 1D electronic dimensionality. The downside is that the chemical formula of this new structure becomes $\text{A}_2\text{B}^+\text{B}^{2+}\text{X}_5$ to maintain the charge neutral (Figure 14c) and cannot meet the strict definition of perovskite structure. Anyway, three compounds $\text{Cs}_2\text{AgPdBr}_5$, $\text{Cs}_2\text{AgPdCl}_5$, and $\text{Cs}_2\text{AgPtCl}_5$ with relatively small bandgap and 1D electronic dimensionality have been successfully synthesized.^[15] The same group also presented a new class of B-site columnar ordered structure $\text{A}_2\text{B}^{2+}\text{B}^{2+}\text{X}_5$ by replacing every two B^+ cations with one B^{2+} cation and one vacancy in $\text{A}_2\text{B}^+\text{B}^{2+}\text{X}_5$ (Figure 14d).^[103] For this class of materials, $\text{Cs}_2\text{Hg}_{0.5}\text{PdCl}_5$, $\text{Cs}_2\text{Hg}_{0.5}\text{PdBr}_5$, and $\text{Cs}_2\text{Hg}_{0.5}\text{PtCl}_5$ were synthesized by the solvothermal method.

5.5. Difficulties to Fabricate HDP Films

The prerequisite for fabricating solar cell devices is the preparation of high-quality thin films. Since most of the stable HDPs are Cl-based compounds (for example, AgCl and CsCl), they suffer from weak solubility in common organic solvents for Pb-based perovskite solar cells, such as DMF and DMSO. This issue hinders the fabrication of thin films by the solution process for various HDPs, including $\text{Cs}_2\text{AgBiCl}_6$, $\text{Cs}_2\text{AgSbCl}_6$, $\text{Cs}_2\text{AgInCl}_6$, $\text{Cs}_2\text{AgFeCl}_6$, $\text{Cs}_2\text{AgTlCl}_6$, etc. It is noted that these HDP crystals can be synthesized from acid (HCl) solution, but acid is not suitable for thin film device fabrication. Meanwhile, only a low concentration of AgCl can be dissolved in HCl solution even under high pressure and high temperature.

For these HDPs with poor solubility, thermal evaporation could be an alternative approach to prepare thin films. In 2018, Liu and co-workers utilized a sequential-vapor-deposition method to

fabricate high-quality and pure-phase HDP $\text{Cs}_2\text{AgBiBr}_6$ thin films for the first time.^[75] AgBr , BiBr_3 , and CsBr were deposited sequentially on top of the substrate layer by layer, and the HDP phase was formed through a diffusion reaction driven by a following thermal annealing process. They emphasized that the sequence of depositing the precursor sources and the nonstoichiometric ratio of precursor materials were essential for forming the pure HDP phase. Attractively, this technique is also feasible for fabricating metal-doped/alloyed HDPs films. For example, Tang and co-workers demonstrated that high-quality Na^+ and Bi^{3+} codoped $\text{Cs}_2\text{AgInCl}_6$ thin films can be deposited by a sequence evaporation process with an optimized molar ratio of precursor materials followed by postannealing.^[100]

The mixed valence Au-based HDPs with ideal bandgaps also suffer from thin film fabrication challenges in two parts: 1) commercially unavailable of the auric (Au^{3+}) iodide salt, as it would decompose into the gold (Au^0) iodide and iodine; 2) the disproportionation of AuI into Au^0 and Au^{3+} . Mathews and co-workers have tried to use AuI as the gold precursor; unfortunately, they were unable to deposit uniform thin films by a conventional solution process.^[73] An interesting approach is to add the reactive polyiodide melt on the surface of MAI/Au bilayer, where iodine vapor could react with MAI to form MAI_3 that could immediately convert the underlying Au film to $\text{MA}_2\text{Au}_2\text{I}_6$.^[73]

5.6. Difficulties to Dope/alloy HDP Films

To improve the weak absorption properties of $\text{Cs}_2\text{AgBiBr}_6$, various metal ions, such as Cu^+ , Cu^{2+} , Fe^{2+} , Fe^{3+} , Tl^{3+} , etc., were successfully doped or alloyed into the crystal/powder and significantly broadened its absorption. But, up to now, except Sb^{3+} , Sn^{2+} , and atomic hydrogen, no other metal dopants have been successfully introduced into $\text{Cs}_2\text{AgBiBr}_6$ thin films.^[21,54,86] We also have mentioned that the order-to-disorder transitions can decrease the bandgap of $\text{Cs}_2\text{AgBiBr}_6$ single crystals; however, this decreased bandgap cannot be kept after films formation, possibly because the condition for the film crystallization during the spin coating process is different from that for single crystal preparation. The most used technique to synthesize high-quality HDPs single crystals is the hydrothermal method, which provides high-temperature and high-pressure conditions with long crystallization and growth time that allow dopants could be partially doped in the lattice or order-to-disorder transitions to occur. However, the crystallization during film preparation by spin coating is much faster and usually completed in seconds or minutes. This issue could potentially be addressed by changing the film fabrication method from spin coating to thermal evaporation, as Na^+ and Bi^{3+} were demonstrated to be alloyed in $\text{Cs}_2\text{AgInCl}_6$ films by a sequential-vapor-deposition method.^[100]

An alternative approach to change the properties of HDP thin films is postmodification. For example, as we mentioned in Figure 9b, mixed-halide HDP $\text{Cs}_2\text{AgBiBr}_{6-x}\text{I}_x$ cannot be obtained by a direct mix of I^- with Br^- in precursor materials. Instead, phase segregation appears in the final product. Wu and co-workers solved this issue and synthesized $\text{Cs}_2\text{AgBiBr}_{6-x}\text{I}_x$ with tunable bandgaps by posttreating $\text{Cs}_2\text{AgBiBr}_6$ thin films with methylammonium iodide (MAI)/isopropanol (IPA) solution via a halide exchange process (Figure 15a,b).^[104] However, such

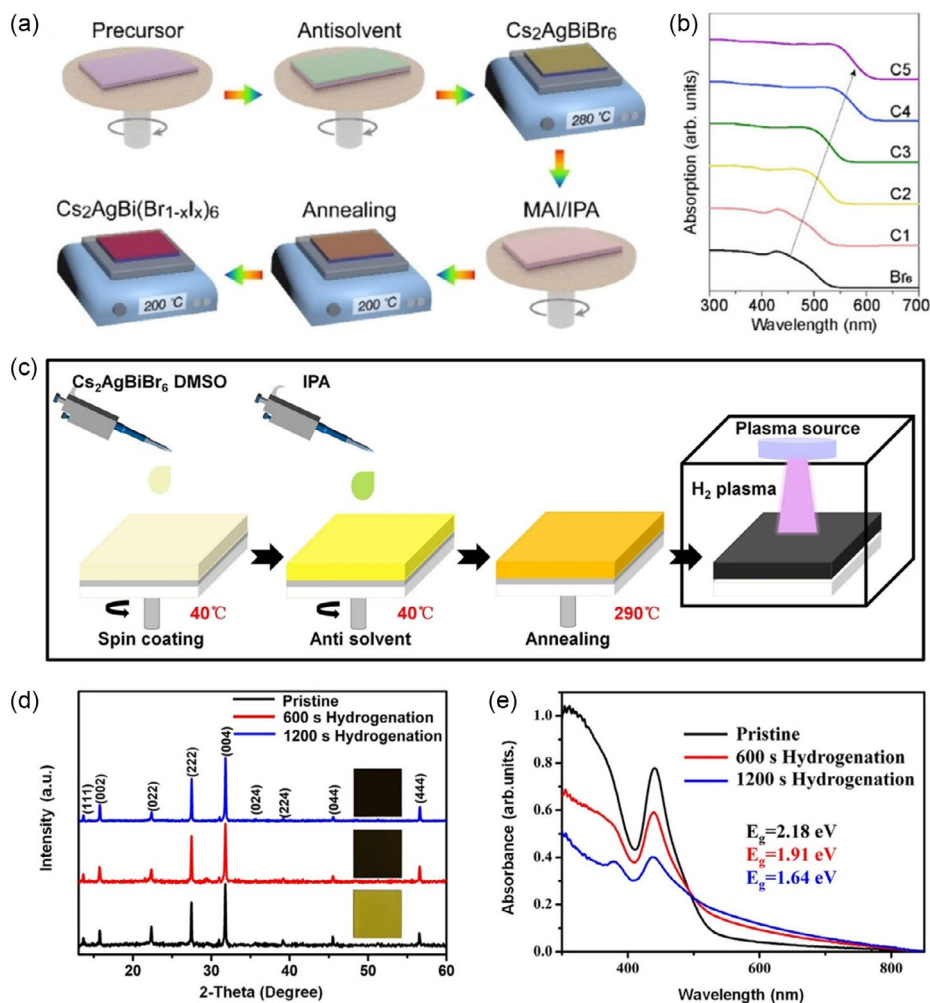


Figure 15. a) Schematic of the posttreatment process with MAI/IPA solution. b) UV-vis absorption spectra of six samples treated with different concentrations of MAI, increasing from left to right (Br₆ to C₅). Reproduced with permission.^[104] Copyright 2021, The Authors. ChemSusChem published by Wiley-VCH. c) The preparation method of Cs₂AgBiBr₆ perovskite films during the hydrogenation treatment in hydrogen gas plasma. d) XRD patterns of the Cs₂AgBiBr₆ perovskite films (insets show the optical pictures of the corresponding Cs₂AgBiBr₆ films). e) UV-vis of the Cs₂AgBiBr₆ perovskite films with different hydrogenation time. Reproduced with permission under the terms of the Creative Commons CC BY license.^[21] Copyright 2022, the Authors. Published by Springer Nature.

mixed-halide HDP films have yet to be explored in solar cell devices. Very recently, Cs₂AgBiBr₆ thin films were hydrogenated by using plasma treatment in a hydrogen (H₂) and argon (Ar) mixed gas environment, as shown in Figure 15c.^[21] The hydrogen-doped Cs₂AgBiBr₆ thin films maintain the cubic phase without any phase transition. Attractively, the color of the films changed from yellow to black with a broadened absorption (Figure 15d,e). More impressively, the solar cells based on this hydrogenated Cs₂AgBiBr₆ thin film show a record PCE of 6.37%. Inspired by the above results, it is worthwhile to devote more efforts to discovering other novel posttreatment strategies to improve the optoelectronic properties of HDP films.

5.7. Contact Issues

Contacts between the perovskite layer and charge transport layers are crucial for high-efficiency solar cells by affecting charge

separation and transfer. Wolfgang and co-workers found that the major bottleneck for high-efficiency Cs₂AgBiBr₆ solar cells comes from the poor selectivity of the contacts and charge transport layers based on the following phenomena.^[74,105] 1) The photocurrents of Cs₂AgBiBr₆ solar cells are highly dependent on the scan rate of the *J*/*V* measurements, possibly related to mobile ions, as shown in Figure 16a. 2) There is a change in the EQE and photocurrent for bias voltages above 0.9 eV, suggesting the nonselective contact (Figure 16b). 3) A weak and significantly redshifted electroluminescence signal observed at around 900 nm indicates high nonradiative recombination (Figure 16c).

Correspondingly, changing the electron transport material (ETM) and HTM are expected to increase the device efficiency. This has been backed up by the fact that the Cs₂AgBiBr₆ devices with mesoporous TiO₂ exhibit a much higher *J*_{sc} than the devices with compact TiO₂,^[17,48] related to the enhanced charge collection and extraction by the mesoporous structure. Changing

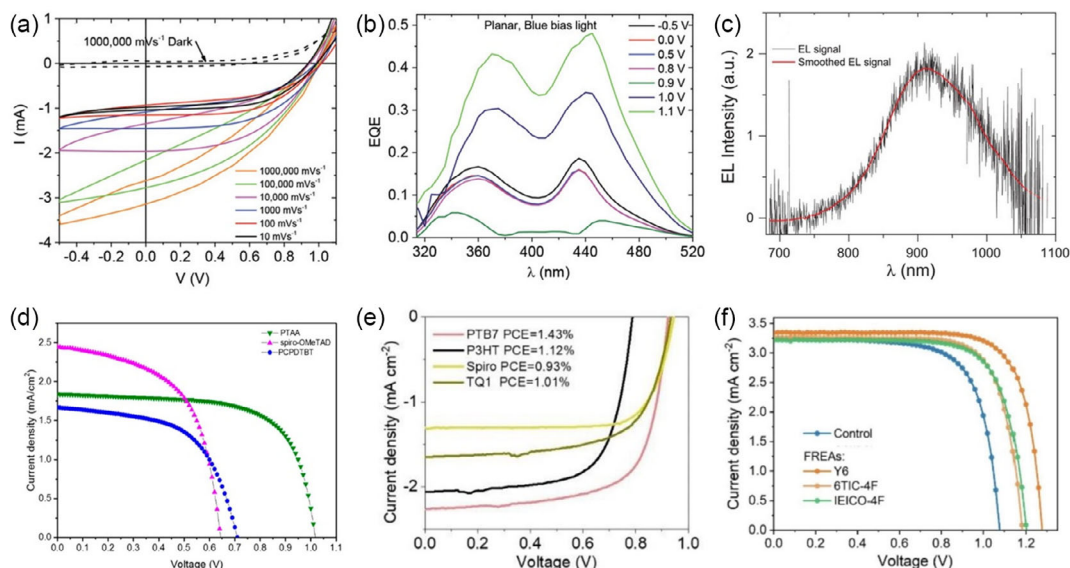


Figure 16. a) J/V loops at different scan rates and after prebias at 1.1 V. The dark curve at 1000 V s^{-1} shows that capacitive effects are still negligible. b) EQE of planar device for various applied voltages. For voltages larger than 0.9 V, the photocurrent changes sign. c) Electroluminescence spectrum of $\text{Cs}_2\text{AgBiBr}_6$ devices. Reproduced with permission.^[105] Copyright 2021, the Authors. Advanced Optical Materials published by Wiley-VCH. d, e) $J-V$ curves for $\text{Cs}_2\text{AgBiBr}_6$ solar cells using different HTMs. (d) Reproduced with permission.^[107] Copyright 2018, American Chemical Society. (e) Reproduced with permission.^[106] Copyright 2021, The Authors. Advanced Functional Materials published by Wiley-VCH GmbH. f) $J-V$ curves of best-performing $\text{Cs}_2\text{AgBiBr}_6$ solar cells with the addition of FREAs. Reproduced with permission.^[108] Copyright 2022, Elsevier B.V.

HTM is more feasible than underlying ETM due to the need of high annealing temperature (over 250°C) for $\text{Cs}_2\text{AgBiBr}_6$ films. $\text{Cs}_2\text{AgBiBr}_6$ solar cells show significantly different device performance based on various HTMs including spiro-OMeTAD, PTAA, PCPDTBT (poly-[2,1,3-benzothiadiazole-4,7-diyl[4,4-bis(2-ethylhexyl)-4Hcyclopenta[2,1-b:3,4-b']dithiophene-2,6-diyl]], PTB7 (poly([4,8-bis[(2-ethylhexyl)oxy]benzo[1,2-b:4,5-b']dithiophene-2,6-diyl][3-fluoro-2-[(2-ethylhexyl)carbonyl]thieno[3,4-b]thiophenediyl]), and P3HT, as shown in Figure 16d,e.^[106,107] Considering some of these HTMs have a similar highest occupied molecular orbital (HOMO) level, different photovoltaic performance possibly result from their different surface recombination and selectivity. Moreover, surface passivation is another important approach for a better contact. Recently, Zhu and co-workers employed the fused-ring electron acceptor (FREA) molecules to reduce surface trap densities and nonradiative recombination in $\text{Cs}_2\text{AgBiBr}_6$ solar cells and enhance V_{oc} from 1.079 to 1.278 V (Figure 16f).^[108]

5.8. Other Challenges

Apart from the challenges discussed above, other possible drawbacks for some HDPs are weak or no PL, high effective carrier masses, short carrier diffusion length, and high defect density. For example, Fe-based, Tl-based, and Au-based HDPs lack obvious PL emission even at low temperatures. The underlying reasons for Tl-based HDPs are mainly due to their parity-forbidden band structure, in which carriers confined to the forbidden region cannot recombine radiatively.^[65] Regarding Fe-based and Au-based HDPs, the mechanism for the nonluminescence is still unclear. Even though PL is an important parameter to

evaluate the device performance, this does not mean that the materials with weak or no PL have no potential for high-performance solar cells. An evidence is that the lead-free compound AgBiS_2 without PL still shows a high PCE of up to 9.17%.^[109] Another issue for Fe-based HDPs is a flat CB mainly derived from highly localized Fe d states, implying relatively high effective carrier masses in these materials. For Au-based HDP $\text{MA}_2\text{Au}_2\text{I}_6$, its poor stability in ambient atmosphere is an obstacle to fabricating high-performance solar cell devices.^[73]

Short carrier diffusion is another concern for HDPs solar cells, especially for HDPs with indirect bandgap property and a low absorption coefficient. For instance, Snaith and co-workers reported that $\text{Cs}_2\text{AgBiBr}_6$ exhibits a n-type behavior with a very short electron diffusion length of only 30 nm.^[46] ascribed to a high density of electron traps in the films. In principle, bismuth/silver antisite defects and bromine vacancies might form deep electron traps^[38]; therefore, Bi-poor/Br-rich conditions possibly deliver films with lower deep-defect densities. Regarding the specific $\text{Cs}_2\text{AgBiBr}_6$ -based solar cells, the major bottlenecks have been well discussed by other reviews.^[74,105] Meanwhile, the developed strategies in Pb-based solar cells to reduce the defect states are worth efforts in HDPs to improve their device performance.

6. Summary and Outlook

HDPs are still in their infancy stage and hold great potential, although various HDPs with attractive optoelectronic properties have not shown promising performance comparable to the dominant Pb-based perovskite solar cells. In this review, we have

summarized the fundamental optical and electrical properties of various stable HDPs candidates for photovoltaics, including Bi-based, Sb-based, In-based, Fe-based, Tl-based, and Au-based compounds. To understand the underlying reasons for current low PCE, we have systematically discussed the main challenges, such as large bandgap, indirect bandgap nature, parity-forbidden transitions, low electronic dimensionality, weak or no PL, poor solubility, difficulties to fabricate and dope/alloy HDP film, contact issues, short carrier diffusion length, and high defect density in thin films. Moreover, we also highlight current solutions and our perspective on resolving these challenges, which are critical to fully exploring the potential of HDPs for photovoltaics. Here, we briefly summarize the above understanding and discuss the potential solutions (Figure 17).

1) In terms of absorption, $\text{Cs}_2\text{AgBiBr}_6$, $\text{Cs}_2\text{AgSbBr}_6$, $\text{Cs}_2\text{Au}_2\text{I}_6$, $\text{MA}_2\text{Au}_2\text{I}_6$, and $\text{Cs}_2\text{AgFeCl}_6$ are the most promising HDP candidates for solar cells due to their relatively small bandgap. Up to now, $\text{Cs}_2\text{AgBiBr}_6$ is the most successful material with a record PCE of 6.37%. Considering that the theoretical limit PCE of $\text{Cs}_2\text{AgBiBr}_6$ is only around 10%, further enhancing the PCE of $\text{Cs}_2\text{AgBiBr}_6$ solar cells requires changing the value and nature of its bandgap. Another attractive HDP is $\text{Cs}_2\text{AgSbBr}_6$ with a bandgap of 1.64 eV. Currently, the device efficiency is only 0.01% due to the presence of a large number of impurities in the film. Therefore, obtaining a pure phase and high-quality $\text{Cs}_2\text{AgSbBr}_6$ thin film is essential. Another interesting part is Sb-based/alloyed HDPs with tunable absorption properties through the oxidation of Sb^{3+} to Sb^{5+} in the structure. Similar to $\text{Cs}_2\text{AgSbBr}_6$, $\text{Cs}_2\text{Au}_2\text{I}_6$ and $\text{MA}_2\text{Au}_2\text{I}_6$ with ideal bandgaps also face the challenge of fabricating high-quality and phase-pure films due to the unavailable AuI_3 salt and the easy formation of metallic Au^0 impurity. In addition, the weak PL and poor stability against moisture of $\text{MA}_2\text{Au}_2\text{I}_6$ also require further efforts. $\text{Cs}_2\text{AgFeCl}_6$ with a direct bandgap of about 1.6 eV is also attractive for single-junction solar cells. However, the poor solubility of precursors is a major challenge for thin film formation. The development of other techniques, such as vapor

evaporation, is required. Furthermore, the absence of PL in Fe-based HDPs may also affect solar cell applications, and the behind reasons remain elusive. In short, as all these reported HDPs are still unsatisfactory for high-efficiency solar cell applications, it is necessary to further modify these host materials. 2) B-site metal doping/alloying is the most common method to modify the optical and electrical properties of HDPs. This approach could tune the bandgap, change the bandgap nature, break the parity forbidden transitions, and increase the electronic dimensionality. Various elements have been fully or partially doped/alloyed in the host HDPs to change their optoelectronic features and further expand the large family of HDPs. However, most of the reported dopants work well on single crystals or powders but fail to dope/alloy into HDPs thin films. This issue may be addressed by employing the thermal evaporation method to fabricate thin films and searching for other suitable dopants. Another drawback is that the metal doping strategy may only have a minimal effect on the indirect bandgap materials with low absorption coefficients. 3) B^+/B^{3+} order to disorder transition is a unique phenomenon in HDPs owing to their rock-salt crystal structure. In principle, increasing the degree of disorder in HDPs could narrow the bandgap, change the indirect bandgap to a pseudo-direct bandgap, and partially increase the electronic dimensionality. An effective approach to change the degree of disorder in the HDPs crystals is high-temperature annealing. But it is still a challenge to precisely control and quantitatively detect the disorder in the materials. In addition, B-site disorder could lead to antisite defects, which are unfavorable for photovoltaic applications. Therefore, the advantages and disadvantages of the order-to-disorder approach need be further evaluated by devices performance. 4) The low solubility of most Cl-based materials makes HDPs a great challenge for thin film fabrication by the solution method. Thermal evaporation is a promising technique for solving this bottleneck and depositing high-quality thin films. Encouragingly, high-quality $\text{Cs}_2\text{AgBiBr}_6$ and Na-alloyed $\text{Cs}_2\text{AgInCl}_6$ thin films have been successfully prepared by the sequential-vapor-deposition approach. It is

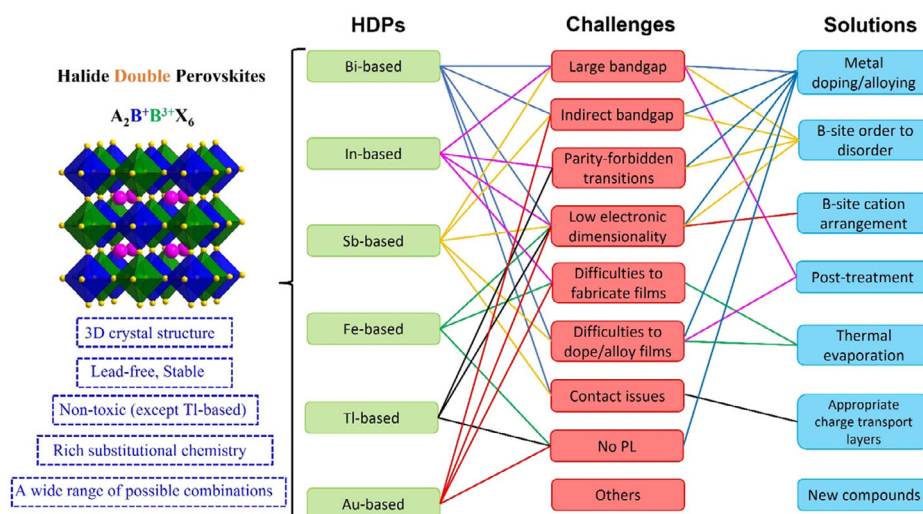


Figure 17. Advantages, challenges, and perspectives in HDPs for photovoltaics. For clarity, the connection related to “other challenges” and “new compounds” two options are hidden here, as all HDPs could face other challenges, and new compounds may address any of these challenges.

highly expected that this technique can be applied to other HDPs, especially for these poorly soluble compounds such as $\text{Cs}_2\text{AgFeCl}_6$, $\text{Cs}_2\text{AgSbCl}_6$, etc. More impressively, the sequential-vapor-deposition method shows promise to precisely control the metal doping in thin films, which is attractive for modifying the optoelectronic properties of the HDPs thin films for high-efficiency solar cells. 5) Posttreatment begins to emerge and deserves more attention to change the opto- and electronic properties of HDPs thin films. Recently, I-rich $\text{Cs}_2\text{AgBiBr}_2\text{I}_4$ thin films with a stable phase and narrowed bandgap have been prepared by the halide exchange process introduced by posttreatment with MAI/IPA solution, even though the film has not yet been applied to solar cell devices. Another breakthrough in the record efficiency of HDPs device was achieved by postdoping atomic hydrogen in $\text{Cs}_2\text{AgBiBr}_6$ films. This is mainly due to the significant J_{sc} boost resulting from the reduction of the film bandgap from 2.18 to 1.64 eV by this posttreatment. Encouraged by the above results, it is worthwhile to devote more efforts to exploring other novel posttreatment strategies to further improve efficiency of HDP-based devices. 6) Last but not least, there is still plenty of room for new HDPs, as several hundreds of new HDPs compounds have not been explored. The structural stability of candidates can be estimated by the new tolerance factor τ , the octahedral factor μ , and the calculated decomposition energy by DFT. Meanwhile, first-principles DFT calculations are powerful to guide experimental synthesis by predicting optoelectronic properties.

Acknowledgements

This work was financially supported by the Swedish Research Council (VR starting grant: 2018-04809), Carl Tryggers Stiftelse, Olle Engkvist Byggmästare Stiftelse, STINT grant (CH2018-7655), Jiangsu Key Laboratory for Carbon-Based Functional Materials & Devices (Soochow University), and the Åforsk (ref.nr 21-32).

Conflict of Interest

The authors declare no conflict of interest.

Keywords

challenges, double perovskites, lead-free perovskites, progress, solar cells

Received: December 19, 2022

Published online:

- [1] A. Kojima, K. Teshima, Y. Shirai, T. Miyasaka, *J. Am. Chem. Soc.* **2009**, *131*, 6050.
- [2] <https://www.nrel.gov/pv/cell-efficiency.html> (accessed: January 2023).
- [3] N. J. Jeon, J. H. Noh, W. S. Yang, Y. C. Kim, S. Ryu, J. Seo, S. I. Seok, *Nature* **2015**, *517*, 476.
- [4] S. D. Stranks, G. E. Eperon, G. Grancini, C. Menelaou, M. J. P. Alcocer, T. Leijtens, L. M. Herz, A. Petrozza, H. J. Snaith, *Science* **2013**, *342*, 341.
- [5] C. Ran, J. Xu, W. Gao, C. Huang, S. Dou, *Chem. Soc. Rev.* **2018**, *47*, 4581.

- [6] N.-G. Park, *Mater. Today* **2015**, *18*, 65.
- [7] M. B. Johnston, L. M. Herz, *Acc. Chem. Res.* **2016**, *49*, 146.
- [8] A. Mei, X. Li, L. Liu, Z. Ku, T. Liu, Y. Rong, M. Xu, M. Hu, J. Chen, Y. Yang, M. Grätzel, H. Han, *Science* **2014**, *345*, 295.
- [9] A. Babayigit, A. Ethirajan, M. Muller, B. Conings, *Nat. Mater.* **2016**, *15*, 247.
- [10] D. Wang, M. Wright, N. K. Elumalai, A. Uddin, *Sol. Energy Mater. Sol. Cells* **2016**, *147*, 255.
- [11] X. Jiang, H. Li, Q. Zhou, Q. Wei, M. Wei, L. Jiang, Z. Wang, Z. Peng, F. Wang, Z. Zang, K. Xu, Y. Hou, S. Teale, W. Zhou, R. Si, X. Gao, E. H. Sargent, Z. Ning, *J. Am. Chem. Soc.* **2021**, *143*, 10970.
- [12] B.-W. Park, B. Philippe, X. Zhang, H. Rensmo, G. Boschloo, E. M. J. Johansson, *Adv. Mater.* **2015**, *27*, 6806.
- [13] M. Chen, M.-G. Ju, A. D. Carl, Y. Zong, R. L. Grimm, J. Gu, X. C. Zeng, Y. Zhou, N. P. Padture, *Joule* **2018**, *2*, 558.
- [14] H. Wu, H. Zhu, A. Erbing, M. B. Johansson, S. Mukherjee, G. J. Man, H. Rensmo, M. Odellius, E. M. J. Johansson, *ACS Appl. Energy Mater.* **2019**, *2*, 5356.
- [15] G. Ji, C. Han, S. Hu, P. Fu, X. Chen, J. Guo, J. Tang, Z. Xiao, *J. Am. Chem. Soc.* **2021**, *143*, 10275.
- [16] A. H. Slavney, T. Hu, A. M. Lindenberg, H. I. Karunadasa, *J. Am. Chem. Soc.* **2016**, *138*, 2138.
- [17] E. Greul, M. L. Petrus, A. Binek, P. Docampo, T. Bein, *J. Mater. Chem. A* **2017**, *5*, 19972.
- [18] J. Yang, C. Bao, W. Ning, B. Wu, F. Ji, Z. Yan, Y. Tao, J. Liu, T. C. Sum, S. Bai, J. Wang, W. Huang, W. Zhang, F. Gao, *Adv. Opt. Mater.* **2019**, *7*, 1801732.
- [19] W. Pan, H. Wu, J. Luo, Z. Deng, C. Ge, C. Chen, X. Jiang, W.-J. Yin, G. Niu, L. Zhu, L. Yin, Y. Zhou, Q. Xie, X. Ke, M. Sui, J. Tang, *Nat. Photonics* **2017**, *11*, 726.
- [20] L. Zhou, Y.-F. Xu, B.-X. Chen, D.-B. Kuang, C.-Y. Su, *Small* **2018**, *14*, 1703762.
- [21] Z. Zhang, Q. Sun, Y. Lu, F. Lu, X. Mu, S.-H. Wei, M. Sui, *Nat. Commun.* **2022**, *13*, 3397.
- [22] H. Lei, D. Hardy, F. Gao, *Adv. Funct. Mater.* **2021**, *31*, 2105898.
- [23] L. Lu, X. Pan, J. Luo, Z. Sun, *Chem. Eur. J.* **2020**, *26*, 16975.
- [24] X. Yang, W. Wang, R. Ran, W. Zhou, Z. Shao, *Energy Fuels* **2020**, *34*, 10513.
- [25] P.-K. Kung, M.-H. Li, P.-Y. Lin, J.-Y. Jhang, M. Pantaler, D. C. Lupascu, G. Grancini, P. Chen, *Sol. RRL* **2020**, *4*, 1900306.
- [26] F. Giustino, H. J. Snaith, *ACS Energy Lett.* **2016**, *1*, 1233.
- [27] V. M. Goldschmidt, *Naturwissenschaften* **1926**, *14*, 477.
- [28] C. Li, X. Lu, W. Ding, L. Feng, Y. Gao, Z. Guo, *Acta Crystallogr., Sect. B: Struct. Sci.* **2008**, *64*, 702.
- [29] C. J. Bartel, C. Sutton, B. R. Goldsmith, R. Ouyang, C. B. Musgrave, L. M. Ghiringhelli, M. Scheffler, *Sci. Adv.* **2019**, *5*, eaav0693.
- [30] Y. Xian, H. Yin, Y. Bao, Y. Xiao, S. Yuan, N. U. Rahman, Y. Yuan, Y. Zhang, X. Meng, S. Jin, W. Li, J. Fan, *J. Phys. Chem. Lett.* **2020**, *11*, 9535.
- [31] Z. Xiao, K. Du, W. Meng, D. B. Mitzi, Y. Yan, *Angew. Chem.* **2017**, *129*, 12275.
- [32] Z. Xiao, Z. Song, Y. Yan, *Adv. Mater.* **2019**, *31*, 1803792.
- [33] E. T. McClure, M. R. Ball, W. Windl, P. M. Woodward, *Chem. Mater.* **2016**, *28*, 1348.
- [34] F. Wei, Z. Deng, S. Sun, F. Zhang, D. M. Evans, G. Kieslich, S. Tominaka, M. A. Carpenter, J. Zhang, P. D. Bristowe, A. K. Cheetham, *Chem. Mater.* **2017**, *29*, 1089.
- [35] W. Lee, D. Choi, S. Kim, *Chem. Mater.* **2020**, *32*, 6864.
- [36] F. Wei, Z. Deng, S. Sun, F. Xie, G. Kieslich, D. M. Evans, M. A. Carpenter, P. D. Bristowe, A. K. Cheetham, *Mater. Horiz.* **2016**, *3*, 328.
- [37] Y. Sun, A. J. Fernández-Carrión, Y. Liu, C. Yin, X. Ming, B.-M. Liu, J. Wang, H. Fu, X. Kuang, X. Xing, *Chem. Mater.* **2021**, *33*, 5905.

- [38] Z. Xiao, W. Meng, J. Wang, Y. Yan, *ChemSusChem* **2016**, 9, 2628.
- [39] F. Ji, J. Klarbring, F. Wang, W. Ning, L. Wang, C. Yin, J. S. M. Figueroa, C. K. Christensen, M. Etter, T. Ederth, L. Sun, S. I. Simak, I. A. Abrikosov, F. Gao, *Angew. Chem.* **2020**, 132, 15303.
- [40] Y. Zhang, Y. Song, Y. Lu, Z. Zhang, Y. Wang, Y. Yang, Q. Dong, Y. Yu, P. Qin, F. Huang, *Small* **2022**, 18, 2201943.
- [41] C. Wu, Q. Zhang, Y. Liu, W. Luo, X. Guo, Z. Huang, H. Ting, W. Sun, X. Zhong, S. Wei, S. Wang, Z. Chen, L. Xiao, *Adv. Sci.* **2018**, 5, 1700759.
- [42] A. Schmitz, L. L. Schaberg, S. Sirotskaya, M. Pantaler, D. C. Lupascu, N. Benson, G. Bacher, *ACS Energy Lett.* **2020**, 5, 559.
- [43] R. Kentsch, M. Scholz, J. Horn, D. Schlettwein, K. Oum, T. Lenzer, *J. Phys. Chem. C* **2018**, 122, 25940.
- [44] K. Du, W. Meng, X. Wang, Y. Yan, D. B. Mitzi, *Angew. Chem., Int. Ed.* **2017**, 56, 8158.
- [45] S. J. Zelewski, J. M. Urban, A. Surrante, D. K. Maude, A. Kuc, L. Schade, R. D. Johnson, M. Dollmann, P. K. Nayak, H. J. Snaith, P. Radaelli, R. Kudrawiec, R. J. Nicholas, P. Plochocka, M. Baranowski, *J. Mater. Chem. C* **2019**, 7, 8350.
- [46] G. Longo, S. Mahesh, L. R. V. Buizza, A. D. Wright, A. J. Ramadan, M. Abdi-Jalebi, P. K. Nayak, L. M. Herz, H. J. Snaith, *ACS Energy Lett.* **2020**, 5, 2200.
- [47] L. Schade, A. D. Wright, R. D. Johnson, M. Dollmann, B. Wenger, P. K. Nayak, D. Prabhakaran, L. M. Herz, R. Nicholas, H. J. Snaith, P. G. Radaelli, *ACS Energy Lett.* **2019**, 4, 299.
- [48] W. Ning, F. Wang, B. Wu, J. Lu, Z. Yan, X. Liu, Y. Tao, J.-M. Liu, W. Huang, M. Fahlman, L. Hultman, T. C. Sum, F. Gao, *Adv. Mater.* **2018**, 30, 1706246.
- [49] R. L. Z. Hoye, L. Eyre, F. Wei, F. Brivio, A. Sadhanala, S. Sun, W. Li, K. H. L. Zhang, J. L. MacManus-Driscoll, P. D. Bristowe, R. H. Friend, A. K. Cheetham, F. Deschler, *Adv. Mater. Interfaces* **2018**, 5, 1800464.
- [50] M. Delor, A. H. Slavney, N. R. Wolf, M. R. Filip, J. B. Neaton, H. I. Karunadasa, N. S. Ginsberg, *ACS Energy Lett.* **2020**, 5, 1337.
- [51] S. E. Creutz, E. N. Crites, M. C. De Siena, D. R. Gamelin, *Nano Lett.* **2018**, 18, 1118.
- [52] J. D. Majher, M. B. Gray, T. A. Strom, P. M. Woodward, *Chem. Mater.* **2019**, 31, 1738.
- [53] F. Wei, Z. Deng, S. Sun, N. T. P. Hartono, H. L. Seng, T. Buonassisi, P. D. Bristowe, A. K. Cheetham, *Chem. Commun.* **2019**, 55, 3721.
- [54] Z. Li, S. R. Kavanagh, M. Napari, R. G. Palgrave, M. Abdi-Jalebi, Z. Andaji-Garmaroudi, D. W. Davies, M. Laitinen, J. Julin, M. A. Isaacs, R. H. Friend, D. O. Scanlon, A. Walsh, R. L. Z. Hoye, *J. Mater. Chem. A* **2020**, 8, 21780.
- [55] T. T. Tran, J. R. Panella, J. R. Chamorro, J. R. Morey, T. M. McQueen, *Mater. Horiz.* **2017**, 4, 688.
- [56] J. Zhou, X. Rong, M. S. Moloakeev, X. Zhang, Z. Xia, *J. Mater. Chem. A* **2018**, 6, 2346.
- [57] S. Wu, W. Li, J. Hu, P. Gao, *J. Mater. Chem. C* **2020**, 8, 13603.
- [58] G. Volonakis, A. A. Haghighirad, R. L. Milot, W. H. Sio, M. R. Filip, B. Wenger, M. B. Johnston, L. M. Herz, H. J. Snaith, F. Giustino, *J. Phys. Chem. Lett.* **2017**, 8, 772.
- [59] W. Meng, X. Wang, Z. Xiao, J. Wang, D. B. Mitzi, Y. Yan, *J. Phys. Chem. Lett.* **2017**, 8, 2999.
- [60] J. Luo, S. Li, H. Wu, Y. Zhou, Y. Li, J. Liu, J. Li, K. Li, F. Yi, G. Niu, J. Tang, *ACS Photonics* **2018**, 5, 398.
- [61] B. Zhou, Z. Liu, S. Fang, H. Zhong, B. Tian, Y. Wang, H. Li, H. Hu, Y. Shi, *ACS Energy Lett.* **2021**, 6, 3343.
- [62] S. Li, J. Luo, J. Liu, J. Tang, *J. Phys. Chem. Lett.* **2019**, 10, 1999.
- [63] H. Yin, Y. Xian, Y. Zhang, W. Chen, X. Wen, N. U. Rahman, Y. Long, B. Jia, J. Fan, W. Li, *Adv. Funct. Mater.* **2020**, 30, 2002225.
- [64] F. Ji, F. Wang, L. Kobera, S. Abbrent, J. Brus, W. Ning, F. Gao, *Chem. Sci.* **2021**, 12, 1730.
- [65] A. H. Slavney, L. Leppert, A. Saldivar Valdes, D. Bartesaghi, T. J. Savenije, J. B. Neaton, H. I. Karunadasa, *Angew. Chem., Int. Ed.* **2018**, 57, 12765.
- [66] S. D. Gupta, *J. Am. Chem. Soc.* **1914**, 36, 747.
- [67] S. Suzuki, M. Tsuyama, *Jpn. J. Appl. Phys.* **2019**, 58, 111002.
- [68] J. Kangsabanik, S. Ghorui, M. Aslam, A. Alam, *Phys. Rev. Appl.* **2020**, 13, 014005.
- [69] . Bhawna, M. Roy, . Vikram, H. Borkar, A. Alam, M. Aslam, *Chem. Commun.* **2021**, 57, 1478.
- [70] W. Shockley, H. J. Queisser, *J. Appl. Phys.* **1961**, 32, 510.
- [71] L. Debbichi, S. Lee, H. Cho, A. M. Rappe, K. Hong, M. S. Jang, H. Kim, *Adv. Mater.* **2018**, 30, 1707001.
- [72] Y. Fan, Q. Liu, Z. Zhang, S.-Y. Lien, Y. Xie, W. Liang, P. Gao, *Chem. Mater.* **2022**, 34, 1544.
- [73] B. Ghosh, B. Febriansyah, P. C. Harikesh, T. M. Koh, S. Hadke, L. H. Wong, J. England, S. G. Mhaisalkar, N. Mathews, *Chem. Mater.* **2020**, 32, 6318.
- [74] W. Tress, M. T. Sirtl, *Sol. RRL* **2022**, 6, 2100770.
- [75] M. Wang, P. Zeng, S. Bai, J. Gu, F. Li, Z. Yang, M. Liu, *Sol. RRL* **2018**, 2, 1800217.
- [76] F. Igbari, R. Wang, Z.-K. Wang, X.-J. Ma, Q. Wang, K.-L. Wang, Y. Zhang, L.-S. Liao, Y. Yang, *Nano Lett.* **2019**, 19, 2066.
- [77] W. Gao, C. Ran, J. Xi, B. Jiao, W. Zhang, M. Wu, X. Hou, Z. Wu, *ChemPhysChem* **2018**, 19, 1696.
- [78] B. Wang, N. Li, L. Yang, C. Dall'Agnese, A. K. Jena, S. Sasaki, T. Miyasaka, H. Tamiaki, X.-F. Wang, *J. Am. Chem. Soc.* **2021**, 143, 2207.
- [79] L. Yang, P. Hou, B. Wang, C. Dall'Agnese, Y. Dall'Agnese, G. Chen, Y. Gogotsi, X. Meng, X.-F. Wang, *Chem. Eng. J.* **2022**, 446, 136963.
- [80] B. Wang, L. Yang, C. Dall'Agnese, A. K. Jena, S. Sasaki, T. Miyasaka, H. Tamiaki, X.-F. Wang, *Sol. RRL* **2020**, 4, 2000166.
- [81] Y. Liu, L. Zhang, M. Wang, Y. Zhong, M. Huang, Y. Long, H. Zhu, *Mater. Today* **2019**, 28, 25.
- [82] D. J. Kubicki, M. Sasaki, S. MacPherson, K. Gałkowski, J. Lewiński, D. Prochowicz, J. J. Titman, S. D. Stranks, *Chem. Mater.* **2020**, 32, 8129.
- [83] X. J. Liu, K. Matsuda, Y. Moritomo, A. Nakamura, N. Kojima, *Phys. Rev. B* **1999**, 59, 7925.
- [84] F. Ji, *Ph.D. Thesis*, Linköping University **2021**.
- [85] A. H. Slavney, L. Leppert, D. Bartesaghi, A. Gold-Parker, M. F. Toney, T. J. Savenije, J. B. Neaton, H. I. Karunadasa, *J. Am. Chem. Soc.* **2017**, 139, 5015.
- [86] K. P. Lindquist, S. A. Mack, A. H. Slavney, L. Leppert, A. Gold-Parker, J. F. Stebbins, A. Salleo, M. F. Toney, J. B. Neaton, H. I. Karunadasa, *Chem. Sci.* **2019**, 10, 10620.
- [87] A. Karmakar, M. S. Dodd, S. Agnihotri, E. Ravera, V. K. Michaelis, *Chem. Mater.* **2018**, 30, 8280.
- [88] F. Ji, Y. Huang, F. Wang, L. Kobera, F. Xie, J. Klarbring, S. Abbrent, J. Brus, C. Yin, S. I. Simak, I. A. Abrikosov, I. A. Buyanova, W. M. Chen, F. Gao, *Adv. Funct. Mater.* **2020**, 30, 2005521.
- [89] Z. Zhang, G. Liu, W. Guo, X. Li, Y. Zhang, C. Wu, B. Qu, J. Shi, Z. Chen, L. Xiao, *Mater. Adv.* **2022**, 3, 4932.
- [90] G. Liu, Z. Zhang, C. Wu, Y. Zhang, X. Li, W. Yu, G. Yao, S. Liu, J. Shi, K. Liu, Z. Chen, L. Xiao, B. Qu, *Adv. Funct. Mater.* **2022**, 32, 2109891.
- [91] A. Luque, A. Marti, *Phys. Rev. Lett.* **1997**, 78, 4.
- [92] D. O. Scanlon, A. Walsh, *Appl. Phys. Lett.* **2012**, 100, 251911.
- [93] J.-S. Park, J.-H. Yang, A. Kanevce, S. Choi, I. L. Repins, S.-H. Wei, *Phys. Rev. B* **2015**, 91, 5.
- [94] J. Yang, P. Zhang, S.-H. Wei, *J. Phys. Chem. Lett.* **2018**, 9, 31.
- [95] W. Yuan, G. Niu, Y. Xian, H. Wu, H. Wang, H. Yin, P. Liu, W. Li, J. Fan, *Adv. Funct. Mater.* **2019**, 29, 1900234.
- [96] Q. Li, Y. Wang, W. Pan, W. Yang, B. Zou, J. Tang, Z. Quan, *Angew. Chem., Int. Ed.* **2017**, 56, 15969.

- [97] W. Ning, X. Zhao, J. Klarbring, S. Bai, F. Ji, F. Wang, S. I. Simak, Y. Tao, X. Ren, L. Zhang, W. Huang, I. A. Abrikosov, F. Gao, *Adv. Funct. Mater.* **2019**, *29*, 1807375.
- [98] A. Karmakar, G. M. Bernard, A. Meldrum, A. O. Oliynyk, V. K. Michaelis, *J. Am. Chem. Soc.* **2020**, *142*, 10780.
- [99] N. R. Wolf, B. A. Connor, A. H. Slavney, H. I. Karunadasa, *Angew. Chem., Int. Ed.* **2021**, *60*, 16264.
- [100] J. Luo, X. Wang, S. Li, J. Liu, Y. Guo, G. Niu, L. Yao, Y. Fu, L. Gao, Q. Dong, C. Zhao, M. Leng, F. Ma, W. Liang, L. Wang, S. Jin, J. Han, L. Zhang, J. Etheridge, J. Wang, Y. Yan, E. H. Sargent, J. Tang, *Nature* **2018**, *563*, 541.
- [101] Z. Xiao, W. Meng, J. Wang, D. B. Mitzi, Y. Yan, *Mater. Horiz.* **2017**, *4*, 206.
- [102] X.-G. Zhao, J.-H. Yang, Y. Fu, D. Yang, Q. Xu, L. Yu, S.-H. Wei, L. Zhang, *J. Am. Chem. Soc.* **2017**, *139*, 2630.
- [103] C. Han, G. Ji, S. Hu, R. Mi, P. Fu, K.-Z. Du, Z. Xiao, *Chem. Mater.* **2021**, *33*, 7106.
- [104] H. Wu, A. Erbing, M. B. Johansson, J. Wang, C. Kamal, M. Odelius, E. M. J. Johansson, *ChemSusChem* **2021**, *14*, 4507.
- [105] M. T. Sirtl, F. Ebadi, B. T. Gorkom, P. Ganswindt, R. A. J. Janssen, T. Bein, W. Tress, *Adv. Opt. Mater.* **2021**, *9*, 2100202.
- [106] H. Wu, Y. Wang, A. Liu, J. Wang, B. J. Kim, Y. Liu, Y. Fang, X. Zhang, G. Boschloo, E. M. J. Johansson, *Adv. Funct. Mater.* **2022**, *32*, 2109402.
- [107] M. Pantaler, K. T. Cho, V. I. E. Quelo, I. García Benito, C. Fettkenhauer, I. Anusca, M. K. Nazeeruddin, D. C. Lupascu, G. Grancini, *ACS Energy Lett.* **2018**, *3*, 1781.
- [108] B. Li, X. Wu, S. Zhang, Z. Li, D. Gao, X. Chen, S. Xiao, C.-C. Chueh, A. K.-Y. Jen, Z. Zhu, *Chem. Eng. J.* **2022**, *446*, 137144.
- [109] Y. Wang, S. R. Kavanagh, I. Burgués-Ceballos, A. Walsh, D. O. Scanlon, G. Konstantatos, *Nat. Photonics* **2022**, *16*, 235.



Fuxiang Ji received his Ph.D. in applied physics from Linköping University in 2021 under the supervision of Prof. Feng Gao. He then joined Prof. Gerrit Boschloo's group as a postdoctoral researcher at Uppsala University in 2022. His current research interests mainly focus on lead-free perovskite materials and related optoelectronic devices.



Gerrit Boschloo is a professor in physical chemistry at Uppsala University, where he leads a research group focusing on perovskite solar cells, dye-sensitized solar cells, and fundamental studies of the semiconductor/electrolyte interface. He received his Ph.D. in 1996 at Delft University of Technology (The Netherlands). He is author of more than 270 peer-reviewed papers (h-index 83) and co-founder of Dyenamo AB.



Feng Wang works as an assistant professor at Linköping University (Sweden). He obtained his Ph.D. from the Chinese University of Hong Kong. He received VINNMER Fellowship (Sweden) in 2017, Marie Skłodowska-Curie Individual Fellowship (European Commission) in 2018, and the Docent in 2022. His research interests focus on solar energy technologies based on lead-based perovskites, lead-free perovskites, and organic transport materials. He has co-authored over 50 peer-reviewed publications in high-impact journals with 7700 citations and the h-index of 40.



Feng Gao is a professor and Wallenberg Academy Fellow at Linköping University in Sweden. He received his Ph.D. from the University of Cambridge (UK) in 2011, followed by a Marie Curie postdoc fellowship at Linköping University. His group currently focuses on research into solution-processed energy materials and devices, mainly based on organic semiconductors and metal halide perovskites.